Czech Technical University in Prague

Faculty of Electrical Engineering
Department of Computer Science
Multi-robot Systems

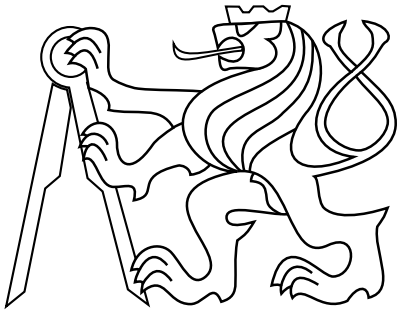

Localization of sources of ionizing radiation using a group of unmanned aerial vehicles

Master's Thesis

Michal Werner

Prague, May 2023

Study programme: Open Informatics
Branch of study: Artificial Intelligence

Supervisor: Ing. Tomáš Báča, Ph.D.

Acknowledgments

First of all, I would like to express my gratitude to my supervisor for all his support, guidance, and valuable advice during this project. Secondly, I am grateful to my classmates and colleagues for the time we spent together in study rooms and libraries, the countless memes we created, and the mutual support we provided each other during challenging exam periods. I am also thankful to my family for their unwavering support throughout my studies. Finally, I would like to express my appreciation to everyone who ensures that the research topic of this work would never be needed in practice and that the "radiation situation remains normal".

Poděkování

Nejprve bych rád vyjádřil svou vděčnost svému vedoucímu za veškerou podporu, vedení a cenné rady během tohoto projektu. Zadruhé děkuji svým spolužákům a kolegům za čas, který jsme spolu strávili v knihovnách a studovnách, nespočet vytvořených memů a vzájemnou podporu během náročných zkouškových období. Jsem také vděčný své rodině za jejich neochvějnou podporu během celých mých studií. Nakonec bych chtěl vyjádřit své uznání všem, kdo se starají o to, aby výzkumné téma této práce nebylo nikdy potřeba v praxi a aby "radiační situace zůstávala normální".

MASTER‘S THESIS ASSIGNMENT

I. Personal and study details

Student's name: **Werner Michal** Personal ID number: **474638**

Faculty / Institute: **Faculty of Electrical Engineering**

Department / Institute: **Department of Computer Science**

Study program: **Open Informatics**

Specialisation: **Artificial Intelligence**

II. Master’s thesis details

Master’s thesis title in English:

Sensor Fusion of Source of Ionizing Radiation onboard a Group of Unmanned Drones

Master’s thesis title in Czech:

Sensorická Fúze Zdrojů Ionizující Radiace Skupinou Bezpilotních Dronů

Guidelines:

The thesis aims to research, design, and implement an algorithm and software method for collaborative sensor fusion of measured ionizing radiation data from a group of unmanned aerial vehicle (UAV) drones. The drones are equipped with a miniature single-detector Compton camera radiation sensor that offers a specific way of sensing a direction towards a source of high-energy gamma radiation. Drones within the group can share the measured data and can collaborate on estimating the position of the radiation source. Moreover, drones can coordinate their behavior to optimize search time. This thesis participates in an industrial project that aims to tackle some of the fundamental and practical questions of homeland security and radiation mapping. The thesis will solve the following points:
1. Get familiar with the MRS UAV system [1] (control, simulation, and experimental validation with UAVs) and the principles of the Compton camera [2] detector.
2. Design and implement a method for the localization of multiple sources of ionizing radiation using the Compton camera data. Utilize data provided by the advisor that were recorded during the experiments with real-world radiation sources [3].
3. Design and implement a search strategy for a small group of UAVs (up to 4) using the data from the sensor fusion software from the previous point.
4. Demonstrate and evaluate the designed estimation method and the search strategy on recorded real-world data and in realistic robotic simulation (Gazebo/ROS [1]).

Bibliography / sources:

[1] Tomas Baca, Matej Petrlik, Matous Vrba, Vojtech Spurny, Robert Penicka, Daniel Hert and Martin Saska. The MRS UAV System: Pushing the Frontiers of Reproducible Research, Real-world Deployment, and Education with Autonomous Unmanned Aerial Vehicles. Journal of Intelligent & Robotic Systems 102(26):1–28, May 2021.
[2] T Baca, P Stibinger, D Doubravova, D Turecek, J Solc, J Rusnak, M Saska and J Jakubek. Gamma Radiation Source Localization for Micro Aerial Vehicles with a Miniature Single-Detector Compton Event Camera. In 2021 International Conference on Unmanned Aircraft Systems (ICUAS). June 2021, 338–346.
[3] S.J. Wilderman, N.H. Clinthorne, J.A. Fessler, and W.L. Rogers. List-mode maximum likelihood reconstruction of Compton scatter camera images in nuclear medicine. In IEEE Nuclear Science Symposium, pages 1716–1720, November 1998.

Name and workplace of master's thesis supervisor:

Ing. Tomáš Báča, Ph.D. Multi-robot Systems FEE

Name and workplace of second master's thesis supervisor or consultant:

Date of master's thesis assignment: **01.02.2023** Deadline for master's thesis submission: **26.05.2023**

Assignment valid until: **22.09.2024**

Ing. Tomáš Báča, Ph.D. Supervisor's signature	Head of department's signature	prof. Mgr. Petr Páta, Ph.D. Dean's signature

III. Assignment receipt

The student acknowledges that the master's thesis is an individual work. The student must produce his thesis without the assistance of others, with the exception of provided consultations. Within the master's thesis, the author must state the names of consultants and include a list of references.

.	
Date of assignment receipt	Student's signature

Declaration

I declare that presented work was developed independently, and that I have listed all sources of information used within, in accordance with the methodical instructions for observing ethical principles in preparation of university theses.

Prague, date ....

Abstract

This thesis presents a method for localizing multiple sources of ionizing radiation using a group of Unmanned Aerial Vehicles (UAVs). These UAVs are equipped with miniature single-detector Compton camera radiation sensors, enabling them to estimate the directions towards high-energy gamma radiation sources. The proposed radiation mapping method (utilizing a Maximum likelihood estimation (MLE) principle) fuses the measurements from the Compton camera sensors to accurately estimate the positions of radioactive sources during the flight. The properties of the used detector are approximated using Monte Carlo simulation techniques. The estimation method is combined with an active search strategy that coordinates future action of the drones in order to improve the quality of estimate of sources position and minimize search time. The proposed solution is evaluated on recorded real world data and in realistic simulator.

Keywords Mobile Robotics, Unmanned Aerial Vehicles, Ionizing Radiation, Sensor Fusion, Compton Camera, Maximum Likelihood Estimation, Timepix

Abstrakt

Tato práce představuje metodu lokalizace více zdrojů ionizující radiace pomocí bezpilotních prostředků (dronů). Tyto drony jsou vybaveny miniaturním detektorem fungujícím na pripcipu jednovrstvé Comptonovy kamery, který umožňuje odhadovat směry k zdrojům vysokoenergetického gama záření. Navržená metoda pro mapování radiace (založená na principu maximální věrohodnosti) kombinuje měření z Comptonových kamer a za letu odhaduje pozice radioaktivních zdrojů. Vlastnosti použitého senzoru jsou odhadnuty pomocí Monte Carlo simulace. Metoda odhadu pozice zdrojů je je kombinována s aktivní prohledávací strategií, která koordinuje pohyb bezpilotních helikoptér za účelem zlepšení kvality odhadu pozice zdrojů radiace a minimalizace času potřebnému k jejich nalezení. Navžené řešení je otestováno na dříve naměřených datech ze skutečných senzorů a pomocí realistického simulátoru.

Klíčová slova mobilní robotika, bezpilotní prostředky, ionizující záření, sensorická fůze, Comptonova kamera, odhad maximální věrohodnosti, Timepix

Abbreviations

GPS Global Positioning System

MLE Maximum likelihood estimation

LKF Linear Kalman Filter

LiDAR Light Detection and Ranging

MiniPIX3 Minipix Timepix3

CS Compton scattering

PE Photoelectric effect

PP Pair production

PET Positron emission tomography

SPECT Single Photon Emission Computed Tomography

FDNPP Fukushima Daiichi Nuclear Power Plant

MLEM Maximum Likelihood Expectation Maximization

EM Expectation Maximization

MAP Maximum A Posteriori

SOE Stochastic Origin Ensemble

TSP Travelling salesman problem

ROS Robot Operating System

SLAM Simultaneous Localization And Mapping

UAV Unmanned Aerial Vehicle

UGV Unmanned Ground Vehicle

CdTe Cadmium telluride

GPU Graphics Processing Unit

Contents

Chapter 1

Introduction

The field of mobile robotics has undergone significant progress in the past decades. Robots are nowadays capable of performing a wide variety of tasks. Such systems can be more efficient than human workers and can replace them in environments that are dangerous for human beings. One possible application for autonomous robots is the mapping and monitoring of ionizing radiation. Radioactive materials are part of our world, and there are several situations when such a need might occur, for example, a disaster in a nuclear power plant or misuse of materials for radiotherapy in medicine. To ensure public safety, we need a method for fast and efficient localization of radioactive sources without the presence of human workers. Unmanned Aerial Vehicles (UAVs) (frequently referred as drones) equipped with appropriate sensors presents a promising solution to this problem. A group of highly mobile UAVs can quickly and autonomously explore large areas and perform measurements needed for precise localization of radioactive sources.

Sensing of ionizing radiation is possible thanks to the variety of sensors, one of which is called the Compton camera. The Compton camera utilizes the Compton scattering effect, which was discovered by Arthur Compton in 1923 [1]. During the Compton scattering, an ionizing photon interacts with an electron and scatters (the photon's direction is changed while part of the photon's energy is transferred to the electron). This principle allows the Compton camera to not only detect the presence of ionizing particles (as common in intensity-based sensors, such as widely known dosimeters), but also reconstruct a set of possible directions from where the photon arrived to the sensor. Thanks to innovations in the field of sensory equipment, Compton camera Minipix Timepix3 (MiniPIX3) became small and lightweight enough to be carried by a small UAV onboard.

Figure 1.1: A small T650 multi-rotor UAV equipped with the MiniPIX3 sensor. Source: [2].

This thesis aims to present a method that performs fusion of sensory data from multiple UAVs (equipped with the Compton camera sensor) in order to localize multiple sources of ionizing radiation. The estimation method is based on the Maximum Likelihood Expectation Maximization (MLEM) algorithm that estimates distribution of sources of ionizing radiation while maximizing likelihood of measured data. The localization of radioactive sources is performed online during the flight. Thanks to the online estimation, the group of UAVs autonomously adapts its actions accordingly in order to increase the precision of the estimate and minimize the search time. The presented data fusion method, as well as the high-level search strategy, are tested in simulations and on prerecorded data from real-world experiments.

1.1 Related work

The remote sensing of ionizing radiation is a very broad topic involving many disciplines, such as medicine, astronomy, industry, public safety or robotics. The overview presented in [3] shows various mobile radiation detection systems, sensors and reconstruction methods that were presented in the past decade. The focus of this thesis is on remote sensing using unmanned vehicles. Several works describing radiation mapping using robots appeared after 2011 when the biggest radioactive accident in past decades happened in Japan. The strong earthquake and following tsunami wave caused several leakages of radioactive substances from Fukushima Daiichi Nuclear Power Plant (FDNPP). The contaminated area of the powerplant was explored by Unmanned Ground Vehicle (UGV)s ([4], [5]) as well as UAVs equipped with different radioactivity sensors ([6]–[10]).

Sensors used for remote monitoring of ionizing radiation can be generally classified into two groups: intensity-based and direction-based. Intensity-based detectors measure only the number of particles recorded in the sensor (particle flux at the sensor's position), whereas the direction-based detectors can also estimate the direction of ionizing radiation. The intensity-based detectors are widely used in remote sensing of ionizing radiation.. The distribution of radioactive material is estimated thanks to intensity measurements acquired at different positions. A group of UGVs remotely sensing contaminated indoor area is presented in [4]. Radiation mapping of a large-scale area around the FDNPP powerplant using an unmanned helicopter equipped with large scintillation intensity-based detectors is shown in [6] and [7]. Multi-rotor UAVs have been used for remote sensing in [11], [12] and [13]. In most of the presented experiments, the UAVs were following predefined trajectories. The radiation mapping was done offline after the flight.

A recent paper [14] presents a method for radiation mapping in the indoor environment. The method is based on estimating the gradient of radiation from multiple intensity-based measurements. The onboard sensors can not only localize the sources of radioactivity but also estimate the energetic spectrum of measured particles and decide which radioactive material is detected. Moreover, the authors have presented an active search path planning method that plans the movement of the drone in order to improve the quality of measurements and shorten the search time.

Work presented in [15] shows a method for radioactivity mapping using intensity-based dosimetric measurements acquired by the same sensor as in this thesis. Each drone measured intensities in multiple directions while statically hovering at it's current position. The direction with the highest intensity was chosen as a direction vector towards the source. These directions vectors acquired at different positions were fused using Linear Kalman Filter (LKF). However, this method is not designed for the localization of multiple sources of radiation.

This thesis focuses on the direction-based sensor — the Compton camera. Radiation mapping around FDNPP using an UAV equipped with a Compton camera is presented in [8]–[10]. In all cases, the platforms were hovering for a certain time above the predefined positions and the radiation images were reconstructed offline after the flight. Work presented in [5] shows a radioactive hotspot localization inside the FDNPP by one UGV equipped with a Compton camera. However, this work focused only on 2D image reconstruction, and the robot was moving only in one direction during the experiment. A 3D localization of a single radioactive source (using an UGV equipped with a Compton camera) is presented in [16]. The authors combine Simultaneous Localization And Mapping (SLAM) method (estimating the 3D map of the environment) with Compton camera measurements. The UGV stops at predefined positions for 5 min and collects around 4000 Compton measurements during the presented simulated experiment. The reconstruction method is based on the iterative MLEM algorithm, the same as in this work. However, the authors of the paper do not specify the details of the proposed MLEM reconstruction method (the system matrix is not further described).

The MLEM reconstruction method was originally developed for nuclear medicine imaging, as described in one of the following chapters. Except few applications in robotic ionizing radiation sensing ([5], [16]), authors of [17] present a handheld device for the localization of radioactive sources. The presented device is composed of an omnidirectional imaging system (capable of acquiring Compton measurements) as well as a Light Detection and Ranging (LiDAR) sensor. The MLEM estimate is combined with a 3D map of the environment, created from LiDAR measurements using a SLAM method. The device weighting 6.3 kg is capable of online estimation of radioactive sources. Another handheld device with an online reconstruction method for Compton camera measurements is presented in [18]. Authors there combine visual data with radiation estimate computed using MLEM method (without evaluating the sensitivity of detection).

In general, one of the key limiting factors is the size of the sensor. There is a tradeoff between the detector's size and the detector's sensitivity. The bigger the sensor is, the more ionizing particles it can measure (given the nature of the radiation). On the other hand, heavy and bulky sensors must be carried by UGVs or UAVs with a sufficient load capacity that reduces their operability. Ground robots can't compete with aerial platforms in the speed of exploration and flexibility. Large aerial platforms (unmanned helicopters) can't fly close to the obstacle due to safety reasons. This motivates the use of small UAVs equipped with small direction-based sensors. The limited sensor's sensitivity can be compensated by the use of multiple UAVs cooperating together on the given task. Moreover, small UAVs can fly closer to obstacles (acquire more measurements) and use the full potential of small agile aerial platforms (acquire measurements from different positions simultaneously and therefore find sources of radiation in a shorter time). This could be achieved thanks to the lightweight MiniPIX3 [19] sensor, which is further described in the next section.

This thesis builds on the work of the MRS group (Faculty of Electrical Engineering, CTU in Prague) that explored the possibilities of MiniPIX3 sensor deployment onboard a small UAVs. Paper [2] presents a multi-robotic approach to an autonomous localization of a compact gamma radiation source. All unmanned aerial vehicles are equipped with a MiniPIX3 sensor same as in our work), which is capable of measuring gamma particles and reconstructing Compton events. The reconstructed Compton cones are used for localization in the following way. In the first phase of autonomous exploration, the UAVs are exploring the area to measure the first Compton cones. After the first eight cones are reconstructed, their intersection is computed using optimization methods (quadratic programming). This initial estimate is then incrementally updated using new measurements. The current estimate is always orthogonally

projected to the newly measured cone. These measurements are fused using LKF. The UAVs are controlled in a way that they encircle the current estimate in order to measure more cones and update the LKF estimate. Using this approach, the group of drones is capable of localizing a single compact source of ionizing radiation. The source can be static or dynamic. However, this iterative method cannot localize multiple sources of radiation. Once the drones detect one source of radioactive particles, they start encircling the current estimate and cannot find other sources in the area.

To the author's best knowledge, there are no related works that solve the task of online autonomous multi-robot mapping of multiple sources of ionizing radiation with the use of a lightweight Compton camera sensor (e.g. MiniPIX3).

1.2 Contributions

The main contribution of this thesis is a novel approach to the localization of multiple compact radioactive sources using measurements from miniature single-layer Compton camera sensors carried onboard UAVs. The main purpose of this thesis is to improve the solution presented in [2] in the following ways: firstly, introduce a new method that could localize multiple sources of ionizing radiation based on the measured Compton cones and, secondly, design high-level planning approach that would control a group of UAVs in order to autonomously explore the whole area and maximize the chance that all sources of ionizing radiation would be detected while estimating their relative emission activity.

1.3 Thesis organization

This thesis is organized as follows. Chapter 2 describes basic properties of ionizing radiation and its interactions with matter, the working principle of the Compton camera and MiniPIX3 sensor. The theoretical background of MLEM estimation method is provided in Chapter 3. Chapter 4 presents the proposed radiation mapping method for a group of UAVs equipped with a MiniPIX3 Compton camera sensor and evaluates properties of the sensor using Monte Carlo simulation. Chapter 5 describes the search strategy that controls the UAVs in order to improve the precision of radiation mapping, acquire more measurements and explore the area of interest. Finally, the proposed methods were tested both in simulation and on real-world data. The results are presented in Chapter 6.

Chapter 2

Preliminaries

2.1 Radioactivity

Radioactivity is a natural phenomenon in which unstable atomic nuclei undergo spontaneous decay, emitting radiation in the form of particles or electromagnetic waves. This process occurs in certain types of atoms, known as radioactive isotopes or radionuclides. The radioactive atom aims to achieve a state of stability by dispensing energy in the form of ionizing radiation. Ionizing radiation refers to any form of radiation with enough energy to remove tightly bound electrons from the orbit of an atom. Among others, radioactive decay releases three main types of ionizing radiation: alpha, beta and gamma.

2.2 Some properties of ionizing radiation

2.2.1 Health risks

Several health risks are associated with ionizing radiation. While traversing the human body, ionizing radiation can interact with living tissues causing damage or mutations of individual cells. In the long-term horizon, exposure to ionizing radiation might cause cancer or even genetic disorders. The severity of health problems depends on the exposure time and dose of absorbed radiation. High doses of ionizing radiation over a short period can cause acute radiation syndrome (radiation sickness), that is manifested by nausea, vomiting, fatigue or even skin burns. High exposure to ionizing radiation also cause several neurological or cardiovascular problems or might lead to death.

2.2.2 Activity

"Activity" is one of the terms used to quantify and describe the properties of radioactive sources and is defined as the number of radioactive decays per second. The unit of activity is called Becquerel (Bq) and belongs to SI[1] units. In other words, if a radioactive source has activity one Becquerel, it means that one unstable nucleus decays per second (on average, since the decay is a stochastic process). The standard definition of activity only measures the rate of decay and does not take into account the type or energy of the radiation involved. However, for the purpose of this thesis, the term activity is used as the number of gamma photons emitted from the source position in any direction per second.

[1] International System of units

2.2.3 Inverse square law

The inverse square law is a fundamental principle that applies to diverse physical phenomena, including radiation. The law describes how the intensity of radiation decreases with increasing distance from the source. The intensity of radiation is inversely proportional to the square distance from the source:

$$intensity \approx \frac{1}{distance^2}. \tag{2.1}$$

For example, doubling the distance to the source means that the intensity decreases to $\frac{1}{4}$. As illustrated in Figure 2.1, this principle comes from the fact that the radiation spreads out over a larger area when the observer is further away from the source. This rapid decrease makes the search for sources of ionizing radiation challenging since it limits the sensing range of the sensors.

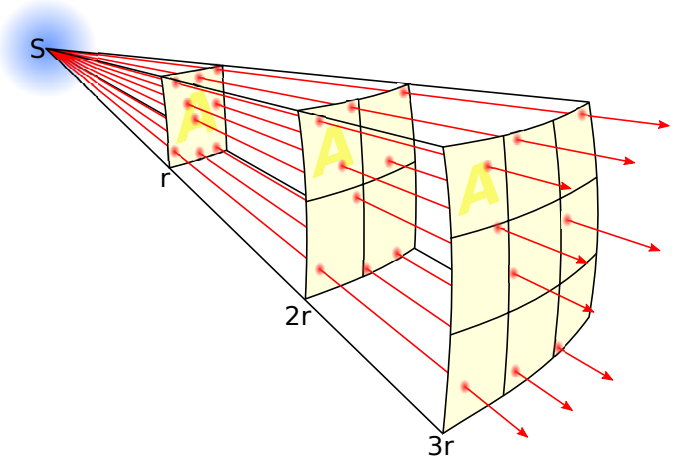

Figure 2.1: An illustration of the inverse square law for the intensity of radiation. Source[2]

2.3 Main types of ionizing radiation

2.3.1 Alpha radiation

Alpha radiation is an emission of positively charged alpha particles consisting of two protons and two neutrons bound together (helium nuclei). This gives alpha particles a significantly larger mass and higher reactivity compared to other types of ionizing radiation, on the other hand, alpha particles interact strongly with matter and can't penetrate far. Alpha particles can travel only a few centimetres in the air and can be blocked by a single sheet of paper or the outer layer of human skin. Because of that, external sources of alpha radiation are generally not considered a significant threat to human health. The limited range of alpha radiation makes it difficult to sense from a distance.

[2] https://commons.wikimedia.org/wiki/File:Inverse_square_law.svg (accessed: 13/05/2023)

2.3.2 Beta radiation

Beta particles are high-energy, high-speed electrons or positrons. Due to their smaller mass and weaker electrical charge, they are generally more penetrating and less reactive than alpha particles and can reach further into materials. Several centimetres thick sheet of aluminium or plastic is typically sufficient to block weak beta radiation. In terms of travel through the air, beta particles have a range of a few meters. Although beta radiation is generally less dangerous than gamma, when particles come into contact with human skin, they can penetrate the outer layers and cause skin burns as the particles disrupt cellular processes.

2.3.3 Gamma radiation

Gamma particles are often produced alongside alpha or beta particles during radioactive decay. Unlike the subatomic particles, gamma radiation of composed of high-energy photons. γ photons are extremely penetrating, can travel long distances in the air and get through most of materials or living tissues thanks to their high energy and lack of charge. Only a thick layer of concrete or lead might block this type of ionizing radiation. These features make gamma radiation significantly more dangerous than alpha and beta. The long-range of gamma radiation, together with its negative effects on human health, motivates the development of methods for the γ radiation sensing and detection.

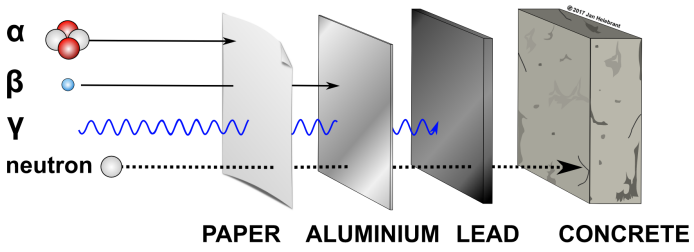

Figure 2.2: Penetrating power of different types of radiation. Source[3]

2.3.4 Cesium-137

Cesium-137 is a radioactive isotope of Cesium and one of the most common by-products of nuclear fission. Cesium-137 is used in radiotherapy in medicine, for calibration of radiation detection equipment in the industry and (most importantly) it is one of the most common fission products by the nuclear fission of Uranium-235, which is used as a fuel in nuclear power plants and in nuclear weapons. Cesium-137 is also the main source of radioactive pollution caused by accidents in Chornobyl (1986) and Fukushima (2011). The half-life (defined as the interval of time required for one-half of the atomic nuclei of a radioactive sample to decay) of Cesium-137 is 30.05 years. Notably, Cesium-137 itself is not a source of γ radiation. Cesium-137 decays by beta emission to metastable Barium-137, which decays almost immediately (with a half-life of about 2.5 minutes) and emits γ photons with initial energy 662 keV. Cesium-137 (with its long half-life, negative health effects, wide usage and high penetrating power

[3] https://openclipart.org/detail/274074/penetrating-power-of-different-types-of-radiation-alpha-beta-gamma-and-neutrons (accessed: 08/05/2023)

of 662 keV photons) is a good candidate for remote sensing. The methods proposed in this thesis have been tested using Cesium-137 radioactive isotope as a source of radiation (during simulated and real-world experiments).

2.4 Interaction of γ radiation with matter

Sensing of γ radiation is possible through interactions of ionizing photons with imaging devices. Type of the interaction depends on both the energy of the incoming photon and the properties of the material it encounters. Several interactions might occur when a high energetic photon travels through matter. The three primary types of interactions include the photoelectric effect, Compton scattering, and electron-positron pair production. Figure 2.3 describes the dominant type of interactions depending on the energy of the incoming photon and the atomic number of the material.

2.4.1 Photoelectric effect and pair production

In Photoelectric effect (PE), alternatively referred to as photoelectric absorption, the γ photon interacts with an orbital electron of the absorbing atom. The photon transfers all its energy to the electron and disappears. As a consequence, the electron exceeds its binning energy and is emitted from the atom. Photoelectric absorption is dominant at lower energies of the incident photon, although it can occur at any photon energy. The Pair production (PP) occurs only if the γ photon has energy exceeding ≈ 1 MeV. In the pair-production, the highly energetic photon interacts with the atom's nucleus. The interaction results in the creation of an electron-positron pair.

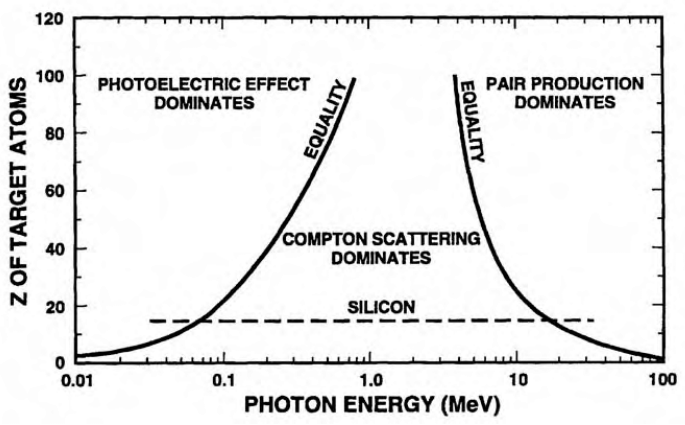

Figure 2.3: Dominant types of interactions for different energy of photon (x-axis) and atomic number of material (y-axis). Source of image: [20]

2.4.2 Compton scattering

The third potential interaction, primarily prevalent at mid-level energies, is Compton scattering. In this process, the γ photon interacts with an electron that is loosely attached to the nucleus. The photon (with its initial energy E_0) transfers a portion of its energy to the electron. As a result of the interaction, the lower energetic photon with energy E_2 is

scattered and emitted in a direction changed by angle β. The energy difference $E_1 = E_0 - E_2$ is transferred to a by-product of the interaction — an electron. The situation is illustrated in Figure 2.4. According to Compton [1], the relation of particle energies and scattering angle β can be expressed as:

$$E_2 = \frac{E_0}{1 + (E_0/m_e c^2)(1 - \cos\beta)}, \tag{2.2}$$

where E_0 is the initial energy of the incoming photon, E_2 is the energy of scattered photon, m_e is the electron rest mass and c is the speed of light in vacuum.

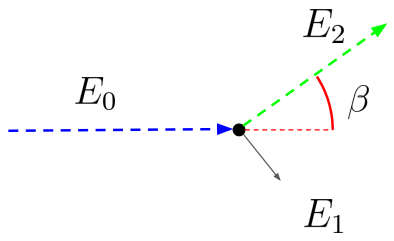

Figure 2.4: An illustration of the Compton scattering. The incident γ photon with energy E_0 (blue) undergoes the Compton scattering. As a result of the interaction, the lower energetic photon (green) with energy E_2 is emitted at angle β. Part of the energy (E_1) is transferred to a by-product of the interaction—the electron (grey).

2.5 Measuring the gamma radiation

Ionizing radiation is mostly unperceivable by human senses yet poses a significant health risk for human beings. Therefore, efficient methods for monitoring and detecting this type of radiation are essential. The primary operating mode of most sensors of radioactivity is counting the number of particles detected, thus estimating the intensity of the particle flux at the sensor's location. However, the dosimetric measurements do not provide information about the direction from which the radiation is emitted. Intensity-only sensors must be relatively large to get accurate measurements (must collect enough interactions and compensate for the stochastic nature of radioactive decay). Moreover, the localization of multiple sources might require many measurements at different positions, which is time-consuming. The direction of incoming γ photons might be deduced using the Compton camera, which is based on the Compton scattering principle.

2.5.1 Compton Camera

The Compton camera is typically composed of two detectors: a scatterer and an absorber. The incident photon with energy E_0 first interacts with the scatterer at position X_1 in the form of Compton scattering. A by-product of the interaction (electron with energy E_1)

is immediately captured by the scatterer, and its position X_1 and energy are recorded. As a result of the interaction, a lower energetic photon with energy E_2 is scattered at (Compton) angle β. The scattered photon then interacts in the form of PE with the absorber. The absorbed energy E_2 and the position of the interaction X_2 are measured and recorded.

The scattering angle β can be reconstructed (following [2]) from equation Equation 2.2 as:

$$\beta = \cos^{-1}\underbrace{\left(1 + m_e c^2 \left(\frac{1}{E_1 + E_0} - \frac{1}{E_0}\right)\right)}_{B}, \tag{2.3}$$

assuming that $0 < B < 1$. Since Compton scattering is a symmetrical phenomenon, the set of possible directions of incoming particles forms a surface of a cone. Such conical surface (denoted as Compton cone) is parametrized by the cone axis **a** (which is a straight line connecting the positions of intersections X_1 and X_2), Compton scattering angle β and origin of the cone X_1. The geometry is illustrated in Figure 2.5.

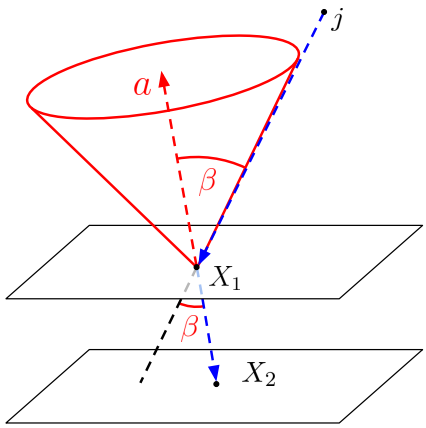

Figure 2.5: Geometry for two-layer Compton camera. The γ particle (emitted at position j) interacts with the first layer of the sensor (the scatterer) at position X_1. A lower energetic photon is scattered at angle β and absorbed by the second layer of the detector (absorber) at position X_2. The reconstructed Compton cone is parametrized by angle β, axis vector a and origin of the cone X_1.

2.5.2 The MiniPIX TPX3 sensor

The MiniPIX TPX3 detector[4] (in the rest of this thesis denoted as MiniPIX3 sensor of ionizing radiation) belongs to the class of semiconductor-based radiation sensors. The MiniPIX3 is composed of a) Timepix3 pixel detector [21], b) the body of the sensor made of a compact block of Cadmium telluride (CdTe) semiconductor material (with dimensions $14 \times 14 \times 2$ mm) and c) the Minipix readout electronics. The whole MiniPIX3 device is very compact and lightweight (the size of the whole MiniPIX3 sensor is only $80 \times 21 \times 14$ mm and it weights 44 g), therefore it can be carried onboard a small UAV. Unlike other devices, the MiniPIX3 sensor can report the recorded γ particles almost in real-time, which allows us to

[4] produced by *Advacam*, https://advacam.com/camera/minipix-tpx3

use it for an active strategy, where autonomous UAVs react according to the measurements acquired during the flight.

Although MiniPIX3 has only one detection layer, it can still be used as a Compton camera. As described in [2] and [19], the incoming ionizing radiation interacts with the matter of the sensor and separates electrons from the CdTe material. The separated electrons are accelerated by a 450 V electric potential towards one facet of the sensor, where the Timepix3 pixel detector is located. The resolution of pixel detector is 256×256 px, each pixel being 55 µm large. The pixel detector can estimate the energy of the absorbed particle and record the time when it was taken with high resolution. Given the measured times of arrival, the coinciding products of Compton scattering might be paired together (assuming that both Compton scattering as well as follow-up photon absorption happened at the same time).

Figure 2.6 depicts the geometry of the MiniPIX3 sensor and the detection process. The x-axis and y-axis coordinates (see Figure 2.6) of the interaction are determined by the position of corresponding pixels. The z-axis coordinate (the depth of interaction in the CdTe block) is unknown. However, the relative z-axis distance of the two coinciding events might be deduced from the times of arrival of the two interactions captured by the pixel detector (given the known speed of electrons in the CdTe material). The absolute z-axis coordinate is not needed since the size of the CdTe block is negligible in the context of the detection task. More technical details related to the sensor operation are provided in [19].

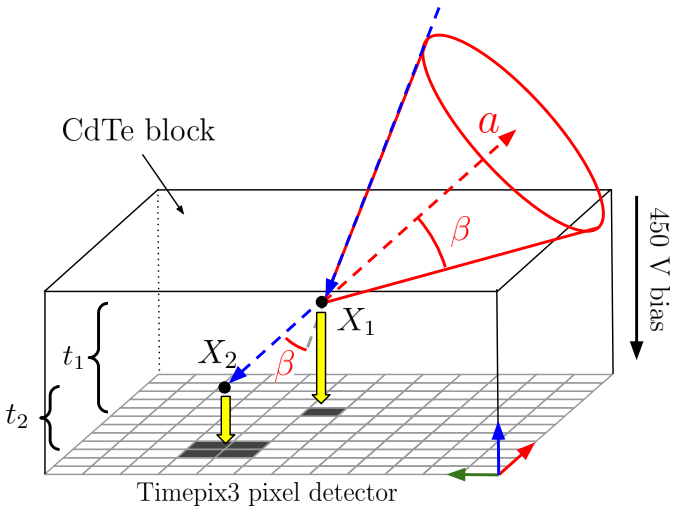

Figure 2.6: An illustration of the detection process inside the MiniPIX3 sensor. The incident photon (blue) scatters at angle β at position X_1. Scattered photon undergoes photoelectric absorption at position X_2. The free electrons (produced by the electron's absorption and scattered photon's absorption) are detected by the Timepix3 pixel detector. 2D positions and energies (E_1, E_2) are recorded. The relative z-axis distance between X_1 and X_2 is deduced from the time difference $t_2 - t_1$ and the known speed of electrons in the CdTe block. The Compton cone (red) is then reconstructed.

(a) The real size of MiniPIX3 sensor. Source: [2]

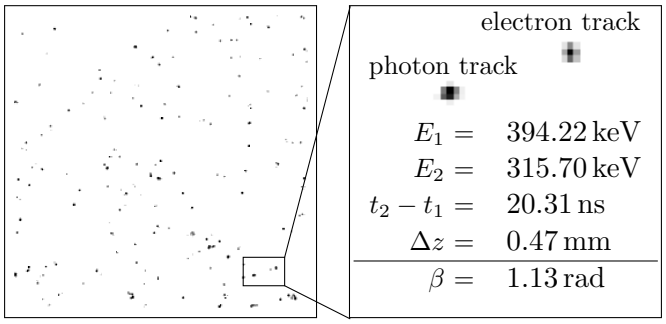

(b) Pixel output of the Timepix3 detector with recorded pair of coinciding events and computed parameters of the Compton cone. Source: [2]

Figure 2.7: The MiniPIX3 sensor and its real size (2.7a) and the illustration of output from Timepix3 pixel detector (2.7b).

2.6 Robot operating system

The Robot Operating System (ROS) [22] is a middleware open-source software framework for robotics applications and research. ROS supports for multiple programming languages, most notably *Python* and *C++*. Individual software modules (called *nodes*) can exchange data through a standardized communication model. The registration of the individual *nodes*, as well as communication between them, is maintained by a central authority called ROS *master*. The main advantage of ROS is its flexibility — multiple *nodes* might be executed independently without restarting the whole program. ROS provides a variety of other useful tools. *TF library* keeps track of multiple coordinate frames over time and provides transformations between them. *Rosbag* is a tool for recording and playing back data collected during the experiments. *RViz* is helpful 3D graphical interface for visualisation and debugging.

2.6.1 ROS communication model

The fundamental ROS communication mechanism used for exchanging messages between different ROS *nodes* is called *topics*. *Topics* are based on a publish-subscribe model, where nodes can either publish data to a topic or subscribe to receive data from a topic. Each topic has a specific data type associated with it. Nodes can publish messages of that data type to the topic, and any subscribed nodes will receive those messages. Topics enable asynchronous communication between different parts of the robotic system, such as data exchange between sensors and onboard computer.

Another important ROS communication concept is called *service*. ROS *services* allow *nodes* to make requests and receive responses to them. Unlike in ROS *topics*, services provide a synchronous request-response communication model. The client node sends its request to a specific service provided by the server node. The server node processes the request and generates a response message, which is sent back to the sender. Such a communication scheme might be used, for example, for triggering some action, requesting a path from the planning node and generally in any situation where a response from the server node is required.

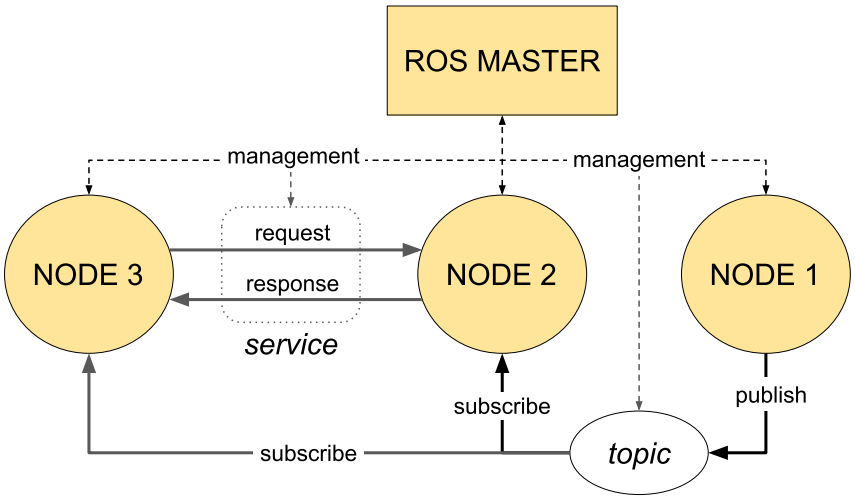

Figure 2.8: Structure of ROS communication model. Individual *nodes* share data using *topics* (publisher-subscriber model) or services (request-response model). The whole communication as well as *node* registration in managed by *master*.

2.6.2 Simulations

The simulations within this project were made using *Gazebo*, an open-source 3D simulator for robotic research. Gazebo is fully compatible with ROS and allows realistic simulations of robotic systems. The ionizing radiation was simulated using *Rospix*[5] simulation package. The simulation process incorporates properties of the environment (air attenuation) as well as the geometry of the sensor and all the underlying principles leading to the detection of an ionizing photon by the Compton camera. The properties of the simulator of ionizing radiation are described in [19].

2.7 MRS UAV system

The proposed high-level search strategy builds on the MRS UAV system[6] [23]. The MRS UAV system is a research-oriented software platform developed at Czech Technical University in Prague. The MRS system is based on ROS and provides full control pipeline for different types of UAVs, including state estimation, sensor fusion, trajectory generation, multi-robot communication, motion planning and feedback control.

[5] available at: `https://github.com/rospix`
[6] available at: `https://github.com/ctu-mrs/mrs_uav_system`

Chapter 3

Methods for Compton imaging

The 3D reconstruction of sources of ionizing radiation poses a challenging problem. The difficulty of this task lies in the fact that the detected γ particle could originate anywhere on the surface of the reconstructed Compton cone. Several methods for Compton imagining have been investigated in the past. This chapter provides a brief overview of such methods and describes the theoretical background of the MLEM algorithm.

3.1 Compton imagining in nuclear medicine

The problem of reconstructing 3D positions of sources of ionizing radiation has been studied in depth in the field of medical imaging, where it is used as a non-invasive method for diagnostics. To give an example: In cancer diagnostics, a small amount of radioactive substance (called a tracer) is injected into the patient's vein. The tracer is absorbed by different parts of the body in varying amounts, which can show areas with abnormal metabolic activity, which is usually the case for cancer cells. The detection of emitted particles and 3D reconstruction of their sources allow doctors to find the location of the tumour in the patient's body.

3.2 Differences

Compton imaging in medical applications typically requires a high resolution of the reconstructed image. The distances between source and detector are small (tens of centimetres), number of measured events is high (tens of thousands and more). The reconstruction process is typically performed offline (all measurements are collected first, and then the algorithms process the data) since there is no need for online estimation, and the processing of measured data might take non-negligible time. The domain of multi-robot radiation mapping has multiple differences compared to the medical field. The distance between the source and detector is much larger (from meters to hundreds of meters). The UAVs have limited payload (hence the detector carried on board must be light and compact). It results in the fact that the number of measurements is much lower (hundreds-thousands detected Compton events). Moreover, we would like to reconstruct the sources of ionizing radiation in real-time. Despite all of these differences, the aim of this work is to get inspiration in the medical field and apply these algorithms to the given problem.

3.3 Reconstruction methods

The reconstruction methods can be divided into two categories: analytical (direct) and iterative algorithms [24].

3.3.1 Analytical reconstruction methods

In analytical methods, the aim is to find a solution directly from the conical projections of reconstructed Compton events. Such a solution might be exact in the continuous model (e.g. computing the exact intersection point of all acquired Compton measurements), yet impractical in real-world applications, where the measurements might be noisy (thus, conical surface projections might not intersect the real position of the source) or where the computational power is limited. To illustrate the difficulties of direct reconstruction methods, the algorithm proposed in [2] estimates the initial hypothesis of the source position as a point that is closest to all measured cone surfaces (which might be considered an analytical method). Finding a solution to the nonlinear least squares problem is computationally demanding and tractable only for a small number of cones. Another example of a simple direct reconstruction method is called back-projection.

Back-projection

Back-projection is one of the simplest reconstruction methods. The Compton cones are projected to the (discretized) space of possible source locations, and each bin records the number of cones intersecting its position. The bins with more intersections are considered as possible source positions. The back-projection for 2D image reconstruction is illustrated in Figure 3.1. The advantage of back-projection method is its simplicity and the fact that it can be easily parametrized when processing a large number of measurements. On the other hand, the back-projection requires a significant number of data in order to make the reconstruction accurate and does not take into account the properties of the detector.

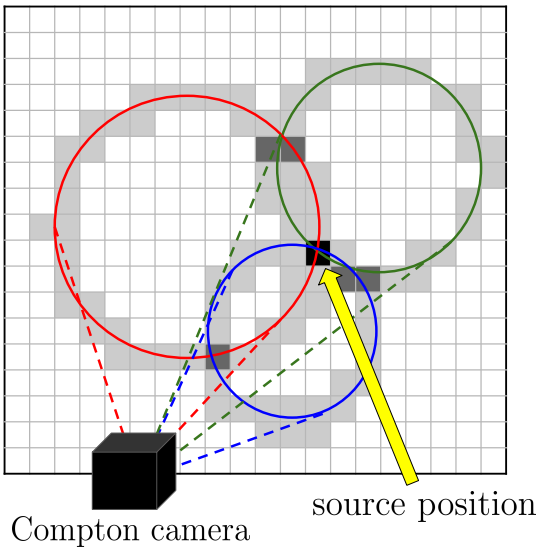

Figure 3.1: Simple back-projection reconstruction method illustrated in 2D. Recorded Compton cones are back-projected to the space of possible source positions. The number of cones intersecting each bin is computed, as illustrated by the white-grey-black cell colours.

3.3.2 Iterative reconstruction methods

The iterative reconstruction methods approximate the positions of sources by iteratively adapting the reconstruction to the measured projections. Each iteration improves the current estimate based on the recorded measurements (the Compton cones), starting from some initial estimate or prior belief of sources distribution. The iterative approach does not provide an exact and unique solution. On the other hand, it is more flexible, can handle noise in the measurements (if it is properly modelled) and is widely used in practice. The iterature [0] describes three main iterative reconstruction methods: Maximum Likelihood Expectation Maximization (MLEM), Maximum A Posteriori (MAP) and Stochastic Origin Ensemble (SOE). MLEM [25], [26], [27] is an iterative algorithm that is based on the maximum likelihood approach. Another approach called MAP [26] is based on the Bayesian approach. It is an extension of MLEM that allows to the incorporation of some prior knowledge about the source distribution or features of the data. SOE is a stochastic algorithm that randomly assigns the origins of the measured events to the conical surfaces. During the course of reconstruction, the origins of events are stochastically moved, and the acceptance of the new event origin is determined by the change in event density. After several iterations, the reconstructed distribution of origins converges to a quasistationary state [28].

The iterative methods were originally developed for Positron emission tomography (PET) and Single Photon Emission Computed Tomography (SPECT) imagining. The PET method is based on positron emission. The emitted positron interacts with electrons in the patient's body, and both particles annihilate. The annihilation produces energy that comes in the form of two gamma photons that go in opposite directions. Detection of these two gamma photons (measured by the detector at the same time) allows us to reconstruct a 3D image of the patient's body. In SPECT, only a single gamma ray is produced. Medical SPECT imagining devices typically acquire measurements from different positions and use collimators to restrict the set of possible directions of incoming gamma radiation. Measured events in PET and SPECT are stored in memory in discrete bins (each bin represents the count of reconstructed particles in a defined time interval or a subset of the image space). The Compton camera events are represented in memory using the list-mode approach. List-mode approach stores measured Compton cones in a list data structure, where each record contains information about the exact arrival time, position and energy of measured interactions. Despite all these differences in the nature of the measurements, the iterative methods were also adapted for Compton imaging.

3.4 Maximum likelihood expectation maximization

The iterative MLEM algorithm is widely used for image reconstruction from the Compton camera data. The algorithm was originally proposed by [25] and later adapted to the Compton camera measurements and list-mode form by [29]. As the name suggests, the algorithm is based on maximizing the likelihood of measured data.

3.4.1 Maximum likelihood estimation

Maximum likelihood estimation (MLE) is a classical approach in machine learning. MLE method is used to estimate the parameters of a probability distribution based on observed data. The goal of MLE is to find the parameter values that make the observed data most

probable under the assumed probability distribution. This is done by calculating the likelihood function, which is the probability of the observed data given a set of parameter values. The likelihood is defined as

$$\mathcal{L}(\boldsymbol{O}|\Phi) = P(\text{observing measurements } \boldsymbol{O} \text{ given parameters } \Phi). \tag{3.1}$$

We want to maximize this expression with respect to the hidden parameters. In other words, we want to find such parameters that fit our observations in the best possible way.

3.4.2 Original MLEM formulation

Let us divide the area of possible sources of radiation into J discrete bins (each indexed with j, where $j = 1 \dots J$). Suppose the binned data space of all measured events is $\mathbf{I}$, divided in I discrete bins indexed with i, $i = 1 \dots I$. The unobservable data space of all not measured events is denoted $\hat{\mathbf{I}}$. Let us define the vector of measurements $\mathbf{Y}$ with elements y_i ($i \in \{1, \dots I\}$) representing the number of particles detected in the corresponding bin i. Let us define matrix $\mathbf{T}$ ($\mathbf{T} \in \mathbb{R}^{I \times J}$), where each position in the matrix is defined as

$$t_{ij} = P(\text{detected in } i|\text{emitted from } j). \tag{3.2}$$

In other words, t_{ij} represents the probability that we observe observation i given that a radioactive particle that caused the observation i has been emitted from position j. Let us assume that the number of photons emitted from one position j is a discrete random variable that follows a Poisson distribution with the expected value λ_j. Our goal is to estimate vector $\boldsymbol{\lambda}$ with elements λ_j ($j \in \{1, \dots, J\}$), each corresponding to the expected intensity of emission from the position j.

Let us assume (for the purpose of the algorithm's derivation) that the matrix $\mathbf{T}$ is known. Then a vector $\boldsymbol{\mu}$ can be defined, where each element of $\boldsymbol{\mu}$

$$\mu_i = \sum_j t_{ij}\lambda_j \tag{3.3}$$

denotes the average number of events measured in bin i. The probability of measuring y_i particles in the measurement bin i with respect to some given average emission intensity $\boldsymbol{\lambda}$ is then expressed as (Poisson distribution):

$$p(y_i|\mu_i) = e^{-\mu_i}\frac{\mu_i^{y_i}}{y_i!}. \tag{3.4}$$

The likelihood of all the measurements (assuming the events to be independent) is

$$\mathcal{L}(\mathbf{Y}|\boldsymbol{\lambda}) = \prod_i p(y_i|\mu_i) = \prod_i e^{-\mu_i}\frac{\mu_i^{y_i}}{y_i!}. \tag{3.5}$$

We want to maximize the likelihood by finding the best possible values of $\boldsymbol{\lambda}$. The maximum likelihood solution is:

$$\boldsymbol{\lambda}_{best} = \underset{\boldsymbol{\lambda}}{\text{argmax}}(\log\, \mathcal{L}(\mathbf{Y}|\boldsymbol{\lambda})). \tag{3.6}$$

Instead of maximizing the product in equation 3.5, it is common to maximize its logarithm since the logarithm is a monotonically increasing function. After taking the logarithm of 3.5

and substitution $\mu_i = \sum_j t_{ij}\lambda_j$, we have the following:

$$\log \mathcal{L}(\mathbf{Y}|\lambda) = \sum_i \left(-\sum_j t_{ij}\lambda_j + y_i \log(\sum_j t_{ij}\lambda_j) - \log(y_i!) \right). \tag{3.7}$$

However, the nonlinear equation 3.7 can not be maximized directly. The solution is to use an iterative Expectation Maximization (EM) algorithm, as proposed in [26].

3.4.3 Expectation maximization algorithm

The EM algorithm was originally described in [30]. It is an iterative algorithm consisting of two steps performed in each iteration — E-step and M-step. The iterations of ac The vector of hidden parameters $\hat{\lambda}^{[l=0]}$ we would like to find is initialized to some starting value using back-projection of the Compton cones or with uniform distribution. The purpose of the E-step is to determine the expectation of the likelihood function given the measurements $\mathbf{Y}$ and the estimation of hidden parameters $\hat{\lambda}^{[l-1]}$ obtained from the previous iteration. Then in the M-step, this expectation is maximized by setting its derivatives (with respect to $\hat{\lambda}^{[l-1]}$) to 0. According to [26], the final formula for iterative MLEM algorithm with binned data is

$$\hat{\lambda}_j^{[l]} = \frac{\hat{\lambda}_j^{[l-1]}}{\sum_i t_{ij}} \sum_{i \in I} \frac{t_{ij} y_i}{\sum_k t_{ik} \hat{\lambda}_k^{[l-1]}}. \tag{3.8}$$

The term $\sum_i t_{ij}$ is called sensitivity of detection s_j and presents the probability that particle emitted at position j is detected by the sensor:

$$s_j = P(\text{detected by the sensor } | \text{emitted from } j) = \sum_i t_{ij}. \tag{3.9}$$

3.4.4 List-mode Maximum Likelihood Expectation Maximization

The list-mode extension of MLEM for the Compton imaging was proposed in [29]. Each measurement bin i in list-mode MLEM consists of only one detected Compton event. Therefore the number of detected events y_i in data bin i is either $y_i = 1$ for the detected event or $y_1 = 0$ when no event was recorded. This simplifies the formula 3.8 to

$$\hat{\lambda}_j^{[l]} = \frac{\hat{\lambda}_j^{[l-1]}}{s_j} \sum_{i \in \mathbf{I}} \frac{t_{ij}}{\sum_k t_{ik} \hat{\lambda}_k^{[l-1]}}. \tag{3.10}$$

We denote as MLEM the list-mode MLEM algorithm for Compton imaging formulated in 3.10 in the rest of the thesis for simplicity. Since only recorded measurements are considered in the list-mode approach, it no longer holds that sensitivity of measurements can be expressed as $s_j = \sum_i t_{ij}$ (summation over all measurement bins i). The sensitivity of detection is then a sum over all events $\{\mathbf{I} \cup \hat{\mathbf{I}}\}$, not only those that were measured, therefore $s_j = \sum_{\mathbf{I} \cup \hat{\mathbf{I}}} t_{ij}$ for Compton imaging.

3.4.5 MLEM algorithm in practical application

The equation 3.10 presents the formulation of the iterative MLEM algorithm maximizing the likelihood of measured data. The system matrix $\mathbf{T}$ and vector of sensitivity values $\mathbf{s} \in \mathbb{R}^J$ with elements s_j depend on the particular geometry of the used sensor and need to be derived individually in each application. The description of system matrix $\mathbf{T}$ and sensitivity vector $\mathbf{s}$ adapted to the presented task is described in Chapter 5.

Several other design choices are to be made in practical applications, such as setting the number of iterations of the MLEM algorithm. The number of iterations in MLEM represents a balance between contrast recovery (quality of reconstruction) and image noise amplification, as stated in [17]. There is no general rule on how to set the optimal number of iterations — it depends on the particular application, level of noise etc. Therefore the number of iterations is set arbitrarily within this project based on the experiments with recorded real-world data.

Chapter 4

Compton imaging for a group of UAVs

The MLEM algorithm for Compton imaging described in the previous chapter has been chosen as a suitable method for data fusion of Compton measurements acquired by a group of UAVs. The motivation for the use of MLEM method is described in section section 4.1. Section section 4.2 presents the adaptation of MLEM to the task of online estimation performed by a group of UAVs. The definition of sensitivity and system matrix is described in section section 4.3 and section 4.4.

4.1 The algorithm of choice

The algorithms for Compton imaging in nuclear medicine (described in the previous chapter) served as inspiration for the imaging method proposed in this thesis. The algorithm of choice is Maximum Likelihood Expectation Maximization (MLEM) (more precisely, its list-mode variant for Compton imaging) for the following reasons.

Firstly, the maximum likelihood approach allows us to deal with factors influencing the measurements (such as air attenuation, the distance between the source and the sensor of ionizing radiation, properties of the sensor and random processes leading to the detection) as well as cope with the stochastic nature of radioactive emission and model both in a probabilistic way. It is also a relatively easy-to-apply and time-proven method in the field of nuclear medicine, which has been applied in the robotic sensing of ionizing radiation.

Secondly, the MLEM can take into account not only "positive" measurements (the Compton events recorded by the sensor) but also "negative" measurements (meaning what was NOT measured by the sensor at the given position in space). Although the radioactive emission, as well as Compton event detection, are stochastic processes, the fact that an UAV flew over some position multiple times and did not measure any Compton event is valuable information that might help improve the estimate. The sensitivity of detection (that is computed during the steps of MLEM algorithm) might serve as a map of coverage of the monitored area. In other words, the sensitivity of detection provides information about how well was which part of the area explored by the drones equipped with the Compton cameras.

Lastly, the algorithm can be easily applied in a scenario with multiple UAVs equipped with Compton cameras. The MLEM method is also computationally tractable under some assumptions (such as a relatively low number of detected events (which holds for the given scenario and type of sensor) or restriction on the set of possible sources locations) and can be evaluated online. The almost real-time estimation is important for active search strategy, where the UAVs may adapt their future actions to the current situation.

4.2 Online MLEM Compton imaging for group of UAVs

4.2.1 Discretization and hidden parameters

As described in Chapter 3, the MLEM algorithm belongs to the class of iterative algorithms that work with discretized space of possible source locations. We assume that the source of ionizing radiation is static and located somewhere on the ground. We further assume that the UAVs are exploring a flat outdoor area without obstacles. Therefore all the potential sources of ionizing radiation are located somewhere on the flat 2D ground plane.

The area of interest (where possible sources of ionizing radiation might be located) is divided into J discrete bins with resolution r, each of them is approximated by its centre position and indexed with j, $j \in \{1, \ldots, J\}$. The set of all collected measurements (the Compton cones) is denoted $\mathbf{I}$. The Compton cones are indexed with i, $i \in \{1, \ldots, I\}$, where I is the total number of cones recorded. The vector of hidden parameters $\boldsymbol{\lambda} \in \mathbb{R}^J$ is defined analogously as in the previous chapter, where each element λ_j represents the expected value of the Poisson distribution, specifying the expected emission rate at position j. The discretization process is illustrated in Figure 4.1.

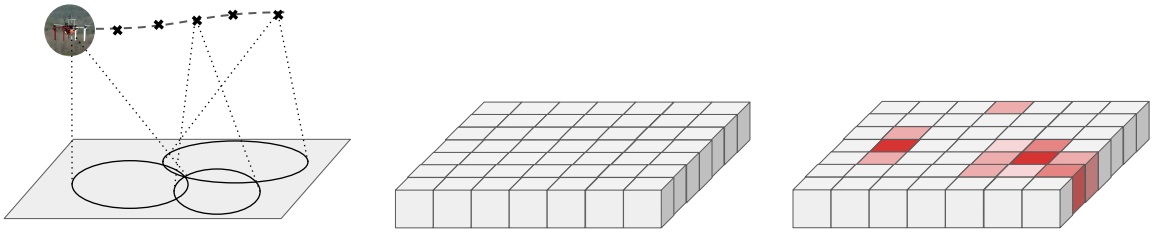

(a) area of interest (b) area discretized with resolution r (c) hidden parameters $\boldsymbol{\lambda}$

Figure 4.1: Illustration of the discretization of the space of possible source positions. The open area without obstacles (a) is discretized into J discrete bins (b), each represented by its centre position and associated with hidden parameter λ_j (c).

4.2.2 Online maximum likelihood estimation

The estimation process proceeds iteratively using the list-mode MLEM algorithm:

$$\lambda_j^{[l]} = \frac{\lambda_j^{[l-1]}}{s_j} \sum_{i \in I} \frac{t_{ij}}{\sum_k t_{ik} \lambda_k^{[l-1]}}, \tag{4.1}$$

where l is the current iteration of the algorithm, λ_j is the hidden parameter for each position j we would like to estimate, t_{ij} is the element of system matrix $\mathbf{T} \in \mathbb{R}^{I \times J}$ and s_j is the sensitivity of detection for the map position j.

As stated before, the MLEM algorithm is typically used as an offline method that proceeds all the measurements at once after the end of the experiment. Medical applications with highly sensitive detectors, together with the short distance between the source and the detector, produce a large number of measurements (tens of thousands and more), and the algorithm typically reconstructs the 3D space with high resolution. The high number of

Compton events results in the fact that the $\mathbf{T} \in \mathbb{R}^{I \times J}$ cannot be stored in the memory during the run of the algorithm and its individual elements t_{ij} are recomputed in every step of the algorithm, which significantly prolongs the computing time. If the instance of the problem (size of the sampled space J and the number of measurements I) is reasonably small, the system matrix $\mathbf{T}$ can be computed only once for each measurement and stored in the memory for future computations, which speeds up the future runs of the MLEM algorithm. Furthermore, the iterations of the MLEM algorithm are formulated as matrix multiplication, which allows parallelization using Graphics Processing Unit (GPU).

Figure 4.2 depicts the workflow of MLEM estimation during the experiment. As the drones fly through the environment, each of the UAVs sample its current position at 5 Hz. The sensitivity of detection vector $\mathbf{s} \in \mathbb{R}^J$ is updated online based on the newly sampled positions. Once the new measurement (Compton cone) i is detected, the vector $\mathbf{t}_i = [t_{i0}, \ldots, t_{ij}, \ldots, t_{iJ}]$ is appended to the system matrix. The iterative MLEM algorithm (4.1) is then repeatedly computed (at 0.5 Hz) using currently available sensitivity vector $\mathbf{s}$, system matrix $\mathbf{T}$ and initialized vector of hidden parameters $\boldsymbol{\lambda}$. The estimate of the distribution of radioactive sources $\boldsymbol{\lambda}$ is therefore updated every 2 seconds, which is technically speaking not in real-time, but the update frequency is sufficient for planning the next actions of the UAVs based on the measured data.

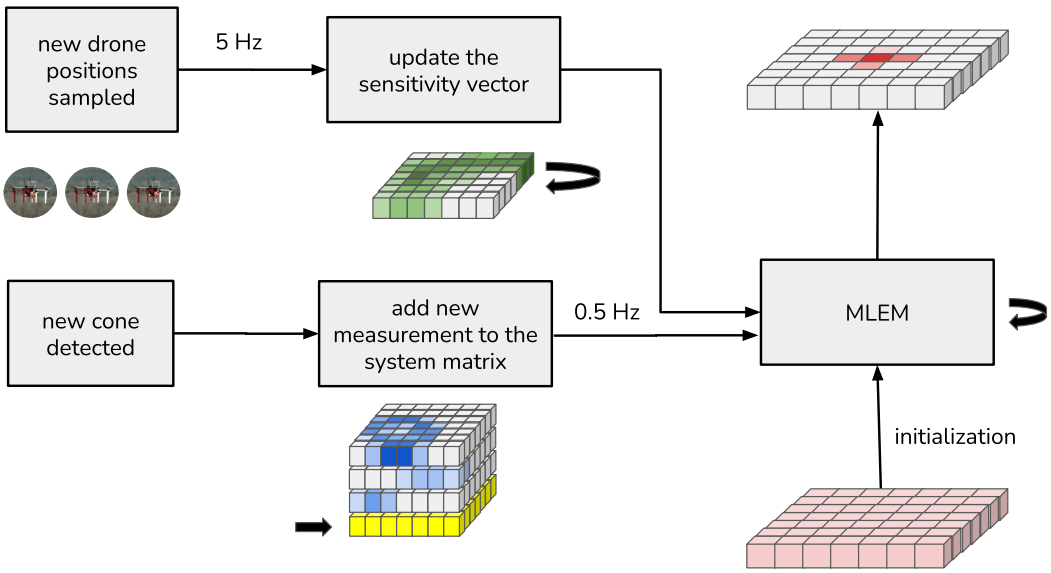

Figure 4.2: Workflow of the (almost) real-time MLEM estimation. The positions of UAVs are sampled at 5 Hz and the sensitivity vector $\mathbf{s} \in \mathbb{R}^J$ (green) is updated online based on newly sampled positions. Once the new Compton cone i is detected by the MiniPIX3 Compton camera, the matrix $\mathbf{T} \in \mathbb{R}^{I \times J}$ (blue) is extended by the new vector $\mathbf{t}_i = [t_{i0}, \ldots, t_{ij}, \ldots, t_{iJ}]$ (yellow). The iterative MLEM algorithm then computes the current estimate of emission intensity $\boldsymbol{\lambda}$ (red) every 2 seconds.

4.3 Sensitivity of detection

The probability of a photon emitted from a given position j to be detected by the Compton camera is called the sensitivity of detection. In the proposed scenario, the sensitivity of the detection can be seen not only as the property of a single Compton camera, but as a sensitivity of the whole multi-robot system, where multiple Compton cameras (mounted on the UAVs) are moving through the environment. The sensitivity can be expressed using conditional probability as

$$s_j = P(\text{detected by the sensor } | \text{emitted from } j). \tag{4.2}$$

A series of random occurrences should happen for a photon to be detected by the Compton camera. First of all, the photon must be emitted from position j towards the sensor surface (emitted in the solid angle subtended by the visible camera surface at the position of the source), not being absorbed by the air along the way. Then the photon should interact with the matter of the sensor in form of Compton scattering. The scattered photon then must be absorbed by the camera in the form of a photoelectric effect. This model is simplified because other random occurrences might happen — for example, the photon might undergo Compton scattering twice in a row, the incident photon might be immediately absorbed, etc. However, we will stick to the proposed simplified model with particles undergoing Compton scattering and then photoelectric absorption consecutively.

The position of the Compton camera sensor is not static in this case. The UAVs carrying the Compton camera are dynamically moving through the environment, with varying speed, position and orientation. Therefore, the positions of the UAVs are sampled in time from UAVs trajectories and denoted as v, where $v \in \{0, \ldots, V\}$ and V is the total number of viewpoints generated by all UAVs during the experiment. The sensitivity of detection is evaluated for each (j, v) pair.

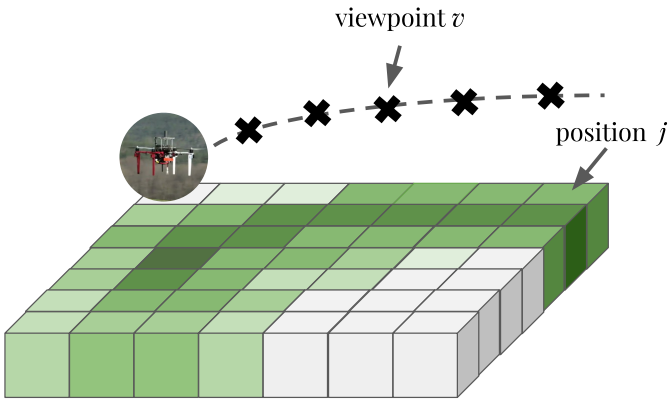

Figure 4.3: An illustration of sensitivity computation. The sensitivity describes the probability that a particle emitted at a given position is measured by the Compton cameras onboard the UAVs. In other words, the sensitivity s_j describes how well explored has been the map position j during the experiment. The trajectory of the UAV is sampled into viewpoints denoted as v. The sensitivity vector $\mathbf{s} \in \mathbb{R}^J$ is illustrated as 2D object just for visualization purposes, although it is a one-dimensional vector.

4.3.1 Probabilistic description

The series of random occurrences for a photon emitted at position j leading to the detection by the Compton camera at camera position v can be described as follows:

$$s_{jv} = (p_{solid\ angle})(1 - p_{air})(p_{compton})(p_{absorption}), \tag{4.3}$$

where $p_{solid\ angle}$ is the probability that the photon is emitted in the solid angle subtended by the visible camera surface (at position j), p_{air} is the probability that a photon is absorbed by the air along the way from emission towards the sensor, $p_{compton}$ is the probability that Compton scattering occurs, and $p_{absorption}$ denotes that scattered photon is absorbed by the detector and measured.

The literature describes several analytical models for computing the sensitivity of the detection. For example, [31] proposed a sensitivity model for multi-layer Compton cameras close to the source. Authors of [32] proposed a simplified model for Compton cameras with negligible size compared to the distance from the source. However, these models are not suitable for the problem tackled in this thesis since the multi-layer Compton camera has different properties than the single-layer Compton camera MiniPIX3. Multi-layer Compton cameras are typically measuring only particles coming from certain directions (from the front side of the camera, perpendicular to its layers). On the other hand, the MiniPIX3 sensor used in this project can potentially measure particles coming from all directions. The sensitivity of the sensor w.r.t. different directions of the incoming particle is unknown and presents a scientific question that needs to be answered to make the MLEM estimate accurate.

Another option presented in the literature is the evaluation of sensitivity using the Monte Carlo simulation. This approach has multiple advantages: it is not necessary to describe all random occurrences inside the detector analytically (which might be complicated and take non-negligible computation time when evaluating a large number of map positions during the experiment). Monte Carlo simulation can be precomputed in advance, and the data can be stored in some data structure that allows fast access to the data, shortening the computation time. Since it is difficult to describe equation 4.3 for MiniPIX3 Compton camera in analytical form (because the probability $p_{compton}$ and $p_{absorption}$ depends on the length of the corresponding intersection of the photon's trajectory with the matter of the detector), we approximate the terms $(p_{solid\ angle})$, $(p_{compton})$ and $(p_{absorption})$ using the Monte Carlo simulation.

4.3.2 Monte Carlo simulation

The idea of Monte Carlo simulation is simple: instead of deriving analytical expression, we will approximate the probabilities by simulating sources of ionizing photons at certain positions and compute how many particles emitted there produced Compton cones in the simulated sensor. The realistic Compton camera simulator described [19] was used as a template and adapted for this particular application.

The position of each simulated source is parametrized by its polar coordinates (angles θ, ϕ and distance d), as shown in 4.4c. Each simulated source emits N particles (in all directions). Since the CdTe semiconductor crystal inside the MiniPIX3 sensor is a symmetrical object, only $\frac{1}{8}$ of the elementary sphere around the sensor needs to be simulated. 4.4b shows the positions of simulated sources, and 4.4a presents their positions in the angle space. We compute the

probability of producing a Compton cone for a particle emitted by a source at the relative position given by polar coordinates (θ, ϕ, d) as

$$p(\text{cone detection})_{(\theta,\phi,d)} = \frac{C_{(\theta,\phi,d)}}{N}, \tag{4.4}$$

where $C_{(\theta,\phi,d)}$ is the number of photons that have undergone the Compton scattering and were consecutively absorbed inside the MiniPIX3 (the CdTe block). We also check if the produced interactions passed outlier detection. The outlier detection consists of the minimum pixel distance of the two recorded interactions on the Timepix chip and energy bounds for a recorded electron with energy E_1 and photon E_2. N is the number of all particles emitted at source position (θ, ϕ, d). Number of emitted particles is set to $N = 10^{10}$, the distance d is set to $d = 1\,\text{m}$ for simplicity. The simulation process is described in algorithm refalg:monte. The results of the simulation are stored in a lookup table:

$$\text{lookup\_table}(\theta_k, \phi_k) = p(\text{cone detection})_{(\theta_k,\phi_k,d=1\,\text{m})}. \tag{4.5}$$

The lookup table is a data structure that allows a fast readout of the stored data. For arbitrary query (θ, ϕ), the lookup table finds the closest key pair (θ_k, ϕ_k) in the angle space and returns the value associated with the key pair.

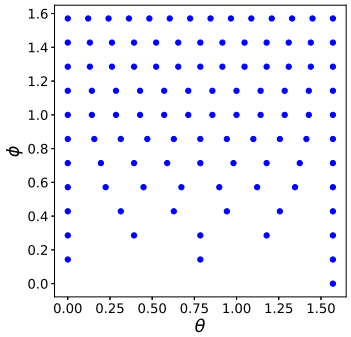

(a) Sampling of the $\frac{1}{8}$ of the unit sphere in the angle space

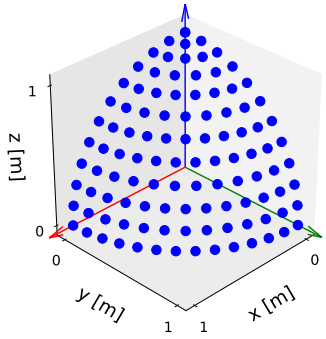

(b) Locations of the simulated sources

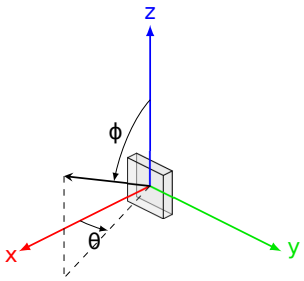

(c) Polar coordinates

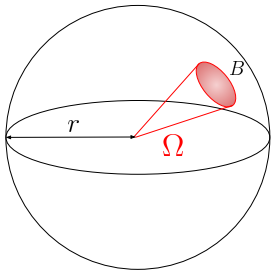

(d) Illustration of the solid angle definition

Figure 4.4: Sampling of $\frac{1}{8}$ of the unit sphere for the Monte Carlo simulation is illustrated in (a) (angle space) and (b) (xyz coordinate system). The polar coordinates determining the direction of incoming particle are presented in (c). Finally, the solid angle definition $\Omega = \frac{B}{r^2}$, where r is the sphere radius and B is the spherical surface area, is shown in (d).

function CREATE_LOOKUP_TABLE(N)
  for $\theta \in (0, \ldots, \frac{\pi}{2})$ **do**
    for $\phi \in (0, \ldots, \frac{\pi}{2})$ **do**
      lookup_table$(\theta, \phi) \leftarrow$ COMPUTE_PROBABILITY(θ, ϕ, N)
    end for
  end for
end function

function COMPUTE_PROBABILITY(θ, ϕ, N)
  $C \leftarrow 0$
  $A \leftarrow N\frac{\Omega_{\theta,\phi,d}}{4\pi}$ ▷ how many of N particles hits the sensor
  $a \leftarrow 0$
  while $a < A$ **do**
    if IS_CONE_MEASURED(θ, ϕ) **then** ▷ Compton cone measured
      $C \leftarrow C + 1$
    end if
    $a \leftarrow a + 1$
  end while
  return C/N
end function

function IS_CONE_MEASURED(θ, ϕ)
  $ray \leftarrow$ SAMPLE_SENSOR_SURFACE(θ, ϕ) ▷ ray inside the sensor after hitting its surface
  if IS_COMPTON_SCATTERING(ray, E_0) **then** ▷ sample if Compton scattering (CS) occured
    $new\_ray, E_1, X_1 \leftarrow$ COMPTON_SCATTERING(ray, E_0)
  else
    return False ▷ No Compton scattering occurred
  end if
  if IS_PHOTOELECTRIC_EFFECT(new_ray, E_1) **then** ▷ Sample if PE occurred
    $E_2, X_2 \leftarrow$PHOTOELECTRIC_EFFECT(new_ray, E_1)
  else
    return False
  end if
  if PASSED_OUTLIER_DETECTION(E_1, E_2, X_1, X_2) **then** ▷ pixel dist. and energy bounds
    return True
  else
    return False
  end if
end function

Figure 4.5: The Monte Carlo simulation pseudocode. For each θ, σ pair, the Monte Carlo method first computes the number of particles emitted towards the visible surface of the detector from the current position (A) out of all simulated particles (N). Then a point for each of A photons is randomly sampled somewhere on the visible sensor's surface, which determines the trajectory of incident photon inside the CdTe sensor's block. The Monte Carlo method counts the number of photons (C) that fulfilled all the following conditions: a) were emitted in the solid angle of the visible sensor's surface, b) undergone the Compton scattering, c) the scattered photon was absorbed, d) the recorded interactions passed the outlier detection filter. The final probability $\frac{C}{N}$ is then stored in the lookup table.

4.3.3 Sensitivity computation

The sensitivity of detection by the sensor placed at sampled position v for map position j is computed as:

$$s_{jv} = \underbrace{e^{-(\mu d_{jv})}}_{(1-p_{air})} \underbrace{\frac{\text{lookup\_table}(\phi_{jv}, \theta_{jv})}{d_{jv}^2}}_{(p_{solid\ angle})(p_{compton})(p_{absorption})}, \tag{4.6}$$

where d_{jv} is the Euclidean distance between map position j and sensor position v, $\mu \approx 0.01\,\mathrm{m}^{-1}$ is the linear attenuation coefficient for 622 keV photons in air, (ϕ_{jv}, θ_{jv}) are the polar coordinates determining the relative position of v and the sensor. The term $\frac{1}{d_{jv}^2}$ in 4.6 ensures that the $p_{solid\ angle}$ (already contained in the lookup_table for $d = 1\,\mathrm{m}$) approximately holds even for distances other than $d = 1\,\mathrm{m}$.

Iterative formula

The equation 4.6 presents the sensitivity computation for one viewpoint v. However, we would like to compute the sensitivity of detection online during the experiment for all the viewpoints previously recorded. Therefore the sensitivity vector is iteratively updated with the newly sampled viewpoints (UAV positions). Let denote $\mathbf{s}^{[t]}$ the sensitivity vector at time t. The initial value of $\mathbf{s}^{[0]}$ is initialized with zeros. Let us denote $V^{[t:t+1]}$ the set of viewpoints that were newly sampled between time t and $t+1$ and needs to be processed.

The sensitivity vector $\mathbf{s}^{[t+1]}$ with elements $s_j^{[t+1]}$ is computed as follows:

$$s_j^{[t+1]} = s_j^{[t]} + \sum_{v \in V^{[t:t+1]}} s_{jv} \Delta_v, \tag{4.7}$$

where the sum $\sum_{v \in V^{[t:t+1]}}$ iterates over all newly processed viewpoints, the term $\Delta_v = t_v - t_{v-1}$ expresses the time difference between current viewpoint v sampled at time t_v and its predecessor (previous viewpoint generated from the trajectory of the same UAV) sampled at time t_{v-1}.

This formulation of sensitivity has multiple advantages. Firstly, the memory requirements for storing the vector $\mathbf{s}$ remain the same during the whole experiment. The values s_j are updated in place. Secondly, the sensitivity is updated online as new sampled trajectories of the UAV arrive. Therefore the computation time scales well with the increasing duration of the experiment. Lastly, it takes into account the time difference between sampled viewpoints Δ_v.

4.4 System matrix

The system matrix $\mathbf{T} \in \mathbb{R}^{I \times J}$ is defined as

$$t_{ij} = P(\text{detected in } i | \text{emitted from } j). \tag{4.8}$$

In other words, it says how likely the photon causing measurement i came from the map position j. The illustration of the system matrix is depicted in Figure 4.6, where the blue colour represents t_{ij} values of the individual cells.

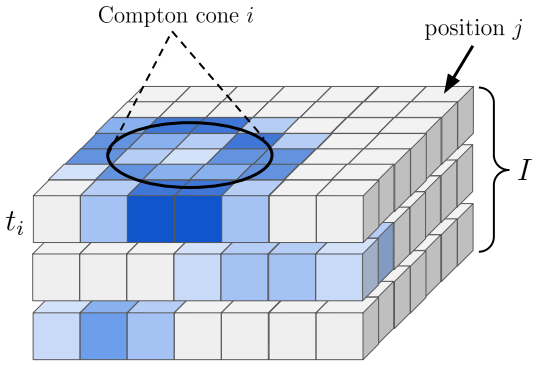

Figure 4.6: System matrix **T**. The blue colour represents the value of t_{ij} in each cell. The system matrix is visualized as 3D matrix just to highlight the relation with newly measured cone i, although it is a two-dimensional matrix of size $I \times J$, where I is the number of recorded Compton cones and J is the size of the map.

The measurement i is composed of multiple components:

$$(\beta_i, \mathbf{v}_i, \mathbf{a}_i, X_1, E_1, X_2, E_2), \tag{4.9}$$

where:

- β_i is the reconstructed Compton angle,
- $\mathbf{v}_i$ is the 3D pose (position and orientation) of the sensor in world coordinates at the time when the event was recorded,
- $\mathbf{a}_i$ is the axis vector of the reconstructed Compton cone,
- X_1 is the position of the first interaction (Compton scattering) inside the detector,
- E_1 is the measured energy of the electron that was created as a side product of the Compton scattering,
- X_2 is the position of the second interaction (absorption) inside the detector,
- E_2 is the measured energy of the absorbed electron.

4.4.1 Probabilistic description

A series of random occurrences should happen for a photon emitted at position j with initial energy E_0 to be detected by the Compton camera as measurement i. The term t_{ij} can be described with probabilities as:

- $p_{solid\ angle}(j, \mathbf{v}_i)$: the probability that the photon is emitted at position j in the right solid angle towards the visible surface of the detector at position $\mathbf{v}_i$,
- $(1 - p_{air}(d_{jv_i}))$: the probability that the photon reaches the detector surface (not being absorbed along the way, where d_{jv_i} is the distance from j to detector pose $\mathbf{v}_i$),
- $\bar{p}_{compton}(j, X_1, E_0, \beta_i)$: the probability that it interacts with the matter of the detector at position X_1 and undergo Compton scattering at angle β_i while losing energy E_1 to the electron that is immediately measured by the detector,
- $\bar{p}_{absorption}(X_1, X_2, E_0, E_1)$: the probability that the scattered photon interacts with the matter of the detector at position X_2, is absorbed and energy E_2 is measured by the detector during the absorption.

Same as in the sensitivity section, the presented model is simplified, and several assumptions are made. It is assumed that the first interaction is a Compton scattering and the second

interaction is the photoelectric effect (absorption) (which might not always be true since other interactions might occur), it is assumed that $E_0 = E_1 + E_2$, etc. Unlike in sensitivity computation (where s_j describes the probability that a photon emitted from j is detected anywhere by the detectors), the elements of system matrix t_{ij} describe the probability that a photon emitted from j was recorded in measurement i, therefore $p_{compton} \neq \bar{p}_{compton}$ and $p_{absorption} \neq \bar{p}_{absorption}$.

4.4.2 Inspiration from literature

The nuclear medicine literature provides multiple models for the system matrix, such as [29] or other models summarized in [33]. However, the model is designed for two-layer Compton camera and for scenarios where the detector size is relatively large compared to the distance to the source. Therefore, the geometry of the Compton camera must be considered. Work presented in [32] described a simplified model for the Compton camera, which size is negligible compared to the distance to the source of radiation (for two-layer Compton camera). The energy measurement uncertainties are approximated using Gaussian distribution. Both of these models do not take into account the effect of environmental attenuation. Despite all of these differences, it served as an inspiration for the proposed approach.

4.4.3 Simplifications of the problem

Efficient evaluation of $\bar{p}_{compton}$ and $\bar{p}_{absorption}$ is challenging since it depends on the length of the incoming and scattered ray inside the detector. In the given scenario, the size of the MiniPIX3 detector is negligible ($14 \times 14 \times 2$ mm) compared to the distance between the detector mounted on the UAV (flying at least 3 m above the ground) and source of radiation. Because of that, modelling $p_{solid\ angle}$ (probability that the particle reaches the detector) and p_{air} (air attenuation) is relatively more important than the accurate modelling of probabilities of events inside the detector. The following simplification is made. The measurement i is represented as

$$(\beta_i, \mathbf{v}_i, \mathbf{a}_i) \tag{4.10}$$

and the measured energies and exact positions of interactions inside the detector are ignored, the Compton camera detector is approximated as a single point with position and orientation v_i. However, the probability of detecting the Compton effect produced by particles incoming from some direction is not uniform for all directions (given the non-uniform shape of the sensor). The lookup table from the previous section (representing the chance that a particle incoming from a specific direction cause any detectable Compton effect, not just the one measured in i) is used to approximate the direction sensitivity of the detector.

4.4.4 System matrix computation

The elements t_{ij} of system matrix $\mathbf{T}$ are computed as:

$$t_{ij} = \underbrace{e^{-(\mu d_{jv_i})}}_{(1-p_{air})} \underbrace{K(\beta_i, E_0)\ h(\delta_{ij}|\sigma, \alpha_{ij})}_{\bar{p}_{compton}} \underbrace{\frac{\text{lookup\_table}(\phi_{jv}, \theta_{jv})}{d^2_{jv_i}}}_{(p_{solid\ angle})(p_{compton})(p_{absorption})}, \tag{4.11}$$

where:

- d_{jv_i} is the Euclidean distance between the map position j and sensor position $\mathbf{v}_i$,
- $\mu \approx 0.01\,\mathrm{m}^{-1}$ is the linear attenuation coefficient for 622 keV photons in air
- $K(\beta_i, E_0)$ is the Klein-Nishina formula (differential cross-section of Compton scattering) representing the probability of Compton scattering at estimated angle β_i for an incoming particle with energy E_0 [33],
- $h(\delta_{ij}|\sigma_j)$ is a Gaussian function (the "blurring factor") representing the uncertainty in angle measurement,
- δ_{ij} is angle difference $|\beta_i - \beta_j|$ (see Figure 4.7),
- σ is standard deviation and α is the minimal angle difference due to discretization noise,
- lookup_table(ϕ_{jv}, θ_{jv}) is the lookup table defined in section section 4.3.

The angular difference δ_{ij} in equation 4.11 comprise the measured Compton cone. If the reconstructed Compton cone (with origin $\mathbf{v}_i$, axis vector $\mathbf{a}_i$ and Compton angle β_i) would perfectly intersect the map position j, then the angular difference would be $\delta_{ij} = 0$, as illustrated in Figure 4.7. However, this holds only for a perfect world without noise.

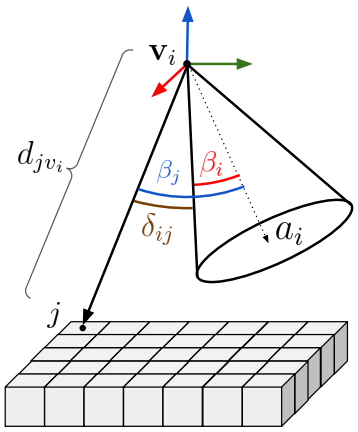

Figure 4.7: An illustration of the measurement i, which is composed of cone origin $\mathbf{v}_i$, axis vector $\mathbf{a}_i$ and Compton angle β_i.

Measurement noise

The real-world measurements are affected by measurement noise. Hence the reconstructed cone might not intersect the real position of emission. The measurement noise might be present in the measured energies E_1 and E_2 (that are affecting the Compton angle β_i , see equation 2.3) as well as in the positions of interactions inside the detector (X_1 and X_2) that are affecting the cone axis $\mathbf{a}_i$. The influence of noise in energy measurement (Compton angle β) is modelled using Gaussian function with standard deviation σ:

$$h(\delta_{ij}|\sigma) = \frac{1}{\sigma\sqrt{2\pi}} e^{-\frac{1}{2}(\frac{\delta_{ij}}{\sigma})^2}. \tag{4.12}$$

If the angle difference is large ($\delta_{ij} < 3\sigma$), then we set $h(\delta_{ij}|\sigma) = 0$. The important question is how to set the parameter σ, that is influencing the width of the function 4.12. The datasheet[1] states that the energy resolution of used Timepix3 pixel detector is 4.5–9.9 kEV. The dependence of angular uncertainties on the energy resolution of two-layer Compton cameras was

[1] Available at: https://advacam.com/camera/minipix-tpx3

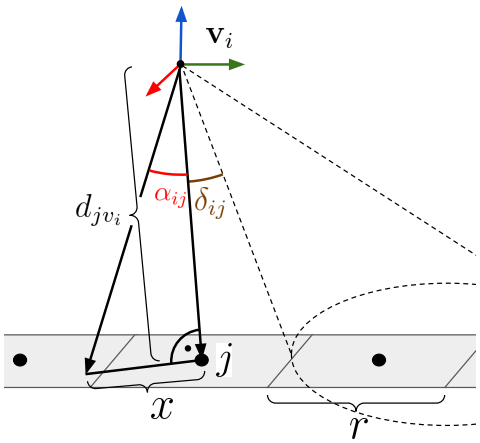

Figure 4.8: Illustration of discretization error. The maximal angle difference caused by discretization error α_{ij} is computed for each map position j.

studied in [34]. The measurement of the energies is not the only source of noise in the detection pipeline. The $h(\delta_{ij}|\sigma)$ function should disperse the conical back-projections in order to tackle other inaccuracies, such as noise in the sensor's position or wrongly estimated axis of the Compton cone. The exact estimation of angular uncertainty (and other sources of noise) is beyond the scope of this thesis. For "proof of concept" demonstration, the value σ was set empirically based on recorded data from experiments with real MiniPIX3 sensors.

Discretization error

Another possible source of noise is the discretization of the area of interest, which is divided into J discrete bins (each represented by its centre position) with resolution r. Even perfectly measured and reconstructed Compton cone might not intersect the real position of emission (meaning δ_{ij} would be non-zero) due to the discretization of J. Let us define maximal error for measurement i and position j caused by discretization as

$$\alpha_{ij} = \arctan(\frac{x}{d_{jv_i}}), \tag{4.13}$$

where d_{jv_i} is the distance between cone origin at position $\mathbf{v}_i$ and map position j and x is the maximal allowed distance between projected cone and discrete position j, $x = r$. The situation is illustrated in Figure 4.8. Taking into account the discretization as well as measurement noise, the term $h(\delta_{ij}|\sigma, \alpha_{ij})$ in equation 4.11 which is projecting the cone to the map positions is defined as

$$h(\delta_{ij}|\sigma) = \begin{cases} 1 & \text{if } \delta_{ij} \leq \alpha_{ij} \\ \frac{1}{\sigma\sqrt{2\pi}} e^{-\frac{1}{2}(\frac{\delta_{ij}}{\sigma})^2} & \text{if } \delta_{ij} > \alpha_{ij} \text{ and } \delta_{ij} \leq 3\sigma_j \\ 0 & \text{otherwise} \end{cases}, \tag{4.14}$$

where α_{ij} is the maximal angle difference caused by discretization error defined in equation 4.13.

Chapter 5

Multirobot search strategy

This chapter presents a multirobot search strategy for a group of UAVs equipped with the Compton camera for online estimation of sources of ionizing radiation, which is based on the MLEM method described in the previous chapter. The search method takes a) the current MLEM estimate of radiation intensity and b) the sensitivity of detection of the whole multi-robot system and compute future actions of the UAVs. We assume that the search mission is performed in open area without obstacles. Objectives and requirements for the proposed search method and as well as its individual parts are presented in this chapter.

5.1 Objectives

5.1.1 Measure as much data as possible

As stated before, the emission of γ particles as well as the detection of Compton events are stochastic processes. The intensity of radioactive emission follows the inverse square law, which means that it decreases as the distance from the source increases. Due to the small size of the detector, large distances between UAVs and sources of ionizing radiation, and the fact that only $\approx 2\%$ of γ particles reaching the detector are detected by the Compton camera (on average), the number of detected events is limited. The accuracy of the MLE method depends on the number of detected Compton events. If the number of detected cones is low, the MLE method might converge to false detections since the particle could originate from any position on the surface of the Compton cone. To accurately localize the sources of ionizing radiation, the UAVs should collect as many measurements as possible. This requires the UAVs to fly as close as possible to the currently most likely source estimates to either confirm or disprove the presence of the radioactive source at the given position. It is also desired that the drones stay in motion (instead of hovering above the points of interest), since measurements from different angles are beneficial for sources localization.

5.1.2 Search for unobserved sources of ionizing radiation

The sensitivity vector $\mathbf{s}$ described in the previous chapter specifies the probability that a particle emitted at certain position is detected. The sensitivity of detection can be therefore seen as

$$s_j = P(\text{detected by the UAV system}|\text{emitted from } j), \tag{5.1}$$

which can be interpreted as a coverage of the area of interest, specifying how much has been point j explored. The autonomous UAVs should control their motion in the way that the whole area is covered. In another words, the minimum value of sensitivity $\min(s_j)$ among all positions in the search space should be as high as possible to increase the chance of observing sources that were not yet detected.

5.1.3 Active search strategy

Two general strategies for exploring an area of interest by a group of autonomous UAVs and for measuring data and estimating sources of ionizing radiation are considered — offline and online. In offline search, the UAVs typically follow predefined paths and collect measurements, that are processed all at once after the flight. In online search, the estimation process is performed online and the UAVs may react accordingly to the current output of the radiation mapping method. Incorporating the output of the mapping method into the feedback control loop might lead to better estimate (since more measurements might be acquired) and fasten the search time. In general, an active search strategy allows the group of UAVs to use its full potential, therefore it is desired for the given task.

5.2 System design description

5.2.1 Task specification

The proposed search strategy is based on the objectives described above — the group of UAVs should autonomously explore the area of interest with no previous knowledge about number, activity or position of sources of ionizing radiation and localize such sources as fast as possible. The operation of the UAVs is divided into two main tasks:

- **exploration**: the drones should explore the area of interest and increase the chance that none of the sources of γ particles would be unobserved,
- **exploitation**: the drones should exploit positions where MLEM mapping method estimated some emission activity to either confirm the hypothesis and collect more measurements or disprove it (in general, increase accuracy of the estimation).

The exploration-exploitation dilemma is solved by dedicating each UAV to either exploration of exploitation task.

5.2.2 Multirobot architecture

The multirobot systems can be classified into two groups: centralized and decentralized. In a centralized approach, a central control unit is responsible for coordinating the actions of all the robots in the network. This centralized system can provide global information to each robot, enabling them to make more informed decisions based on the overall state of the system. In decentralized system, each robot operates independently, making decisions based on local information and communication with other robots in the network.

The centralized multirobot architecture is used in this project. The visualization of the system architecture is presented in Figure 5.1. The UAVs are communicating via wireless **Wifi** network. The amount of information shareable via such network is limited. Therefore all the MLEM computations and running on a ground station and the UAVs and ground station share the minimal amount of information possible. All the UAVs send its current position and future position as a custom ROS message (with frequency 5 Hz) and newly detected Compton cones. The ground station processes the measurements and command the UAVs by sending non-colliding path for each of them via the wireless network. The centralized approach have several advantages in this scenario: the MLEM estimate is computed at once, not requiring to share or merge the map with other UAVs via the wireless network or run the estimation

onboard each drone separately. The centralized task allocation and path planning is much more straightforward compared to the decentralized approach, where the agents would need to negotiate between each other.

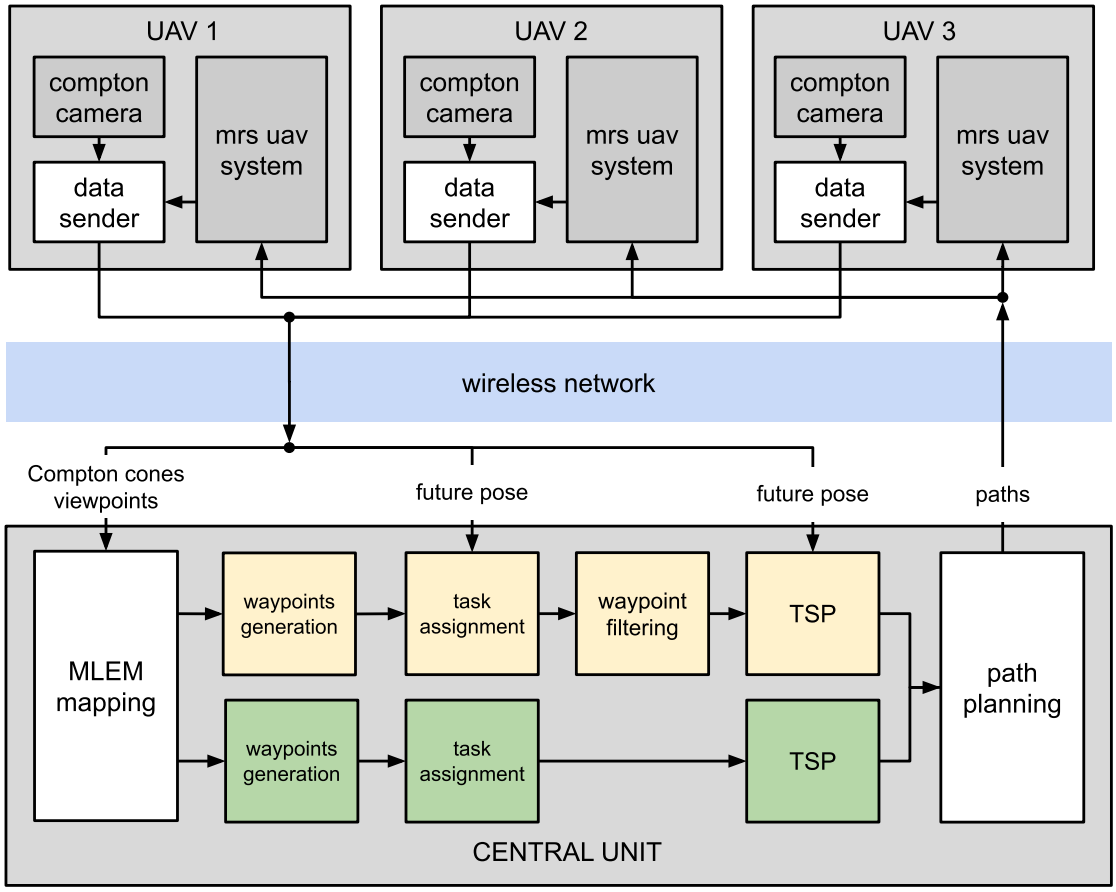

Figure 5.1: The system architecture diagram. The search and planning method is composed of MLEM radiation mapping node, waypoint generation, task assignment, waypoint filtering, optimal sequence deduction using Travelling salesman problem (TSP) and path planning. The exploration (green) and exploitation (yellow) waypoints are processed separately.

5.3 Search and planning strategy description

The central method responsible for search and planning strategy is composed of multiple components: **MLEM mapping**, **waypoints generation**, **task assignment**, **waypoint filtering**, optimal sequence of waypoints deduction using **Travelling salesman problem (TSP)** and **path planning**. Each step of the system design is visualized in Figure 5.2.

The MLEM mapping node produces the current estimate of source intensities $\boldsymbol{\lambda}$ and current estimate of sensitivity $\mathbf{s}$, which are taken as input of the waypoint generation node (5.2a). The waypoint generation node assigns weights to the waypoints (5.2b). The filtered waypoints are then assigned to individual UAVs (5.2c). To avoid revisiting the same point multiple times while ignoring others, the recently visited waypoints are filtered out in the next step (5.2d). All points assigned to one UAV are connected into an optimal sequence (starting

at the future position of the drone) using TSP (5.2e). Finally, non-colliding paths are planned for all UAVs (5.2f). The more detailed description of each individual step follows in the next sections.

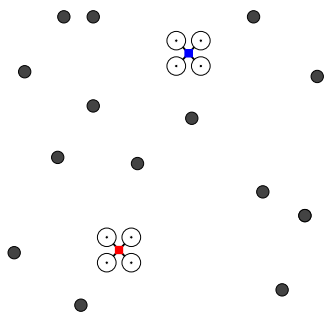

(a) **waypoint generation** - detected local maxima of MLEM estimate

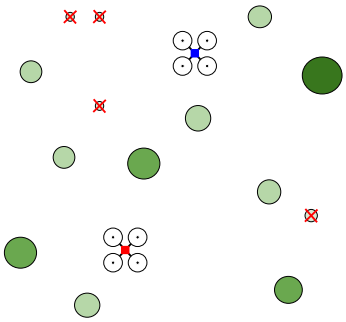

(b) **waypoint generation** - weighing and filtering

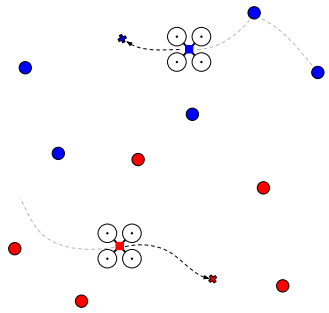

(c) **task assignment** - assigning waypoints to UAVs

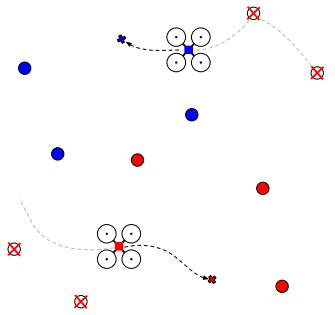

(d) **waypoint filtering** - removal of recently visited waypoints based on short-term sensitivity

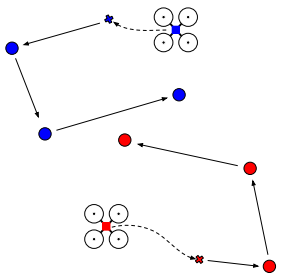

(e) **TSP** - optimal sequence determination

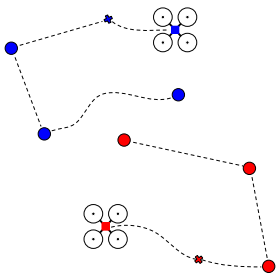

(f) **path planning** - find non-colliding paths connecting the waypoints

Figure 5.2: Individual steps of the system architecture. Waypoints are generated based on the current MLEM estimate (a). The weighted and filtered waypoints (b) are then assigned to individual UAVs (c). The system prioritizes waypoints that were not recently visited (d). Finally, an optimal sequence of waypoints for each UAV is determined using TSP (e) and the sequence of waypoints is passed to the planning node, that finds non-colliding paths for all UAVs (f).

5.4 Waypoints generation

The waypoint generation method generates waypoints that should be visited by the UAVs to get more measurements and further explore the area of interest. As illustrated in Figure 5.1, the waypoint generation process is different for UAV dedicated to exploitation or exploration.

5.4.1 Exploitation

The exploitation waypoints are generated in order to visit positions where the MLEM method estimated possible sources of ionizing radiation to either confirm or disprove the presence of a radioactive source there.

Local maxima filter

The current estimate of ionizing radiation sources positions serves as an input for the waypoint generation method. The map estimated by the MLEM method is processed and local maxima of the map are detected. Local maximum is a cell in the discretized map that has the highest value among all cells in its neighborhood. The size of the sliding window determining the neighborhood of each cell is a parameter that can be set. The local maxima filter is illustrated in Figure 5.3.

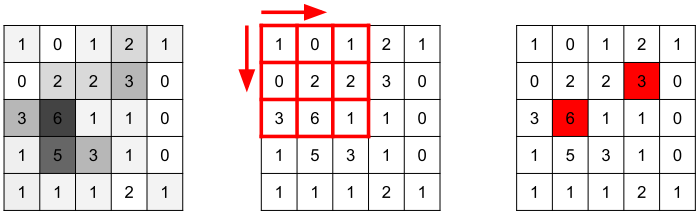

(a) input of the filter (b) filter window size 3 (c) detected local maxima

Figure 5.3: Local maxima filter demonstration. The filter takes the current MLEM estimate as an input (a) and detects cells that are greater than all cells in its neighbourhood (c), which is specified by the filter window of a predefined size (b).

Waypoint weighting and filtration

The waypoints associated with local maxima are weighted using following formula:

$$w_{j_{weight}} = \frac{\lambda_j}{s_{j_{normalized}}}, \tag{5.2}$$

where $s_{j_{normalized}} = \frac{s_j}{\max\limits_j(s_j)}$ is a sensitivity value normalized to range $[0, 1]$. The purpose of the weighting step is following: it should prioritize the waypoints (local maxima) that are less explored (the sensitivity value is small compared to other waypoints). The list of possible waypoints is then sorted from the highest $w_{j_{weight}}$ to the lowest. Top n waypoints based on

the $w_{j_{weight}}$ are propagated further in the algorithm, the rest is ignored (parameter n is set to $n = 10d$, where d is number of drones used for exploitation). The aim of the filtering step is to remove the local maxima that were caused by noise in the MLEM estimation.

5.4.2 Exploration

The task is to explore the map positions that have low sensitivity values (the probability that particle emitted from such position to be detected is low). The process of generating waypoints for exploration is illustrated in Figure 5.4. The sensitivity vector **S** is downsampled by a mean filter with the stride equal to the filter window size. The positions in the downsampled map are then sorted based on the mean sensitivity value. Arbitrary percentage p of the map poses with lowest sensitivity values is taken and exploration waypoints are generated in the centers of such downsampled map positions, as shown in 5.4c for $p = 25\%$.

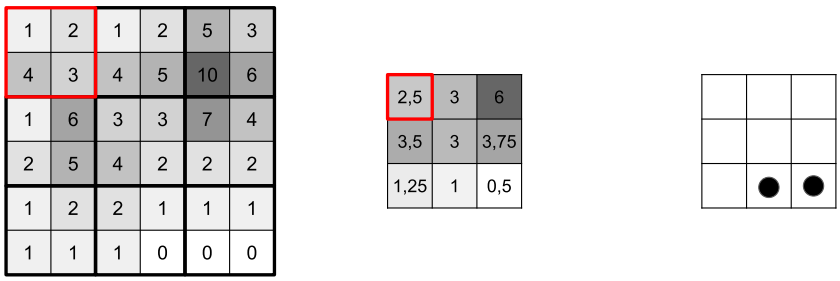

(a) input vector **S** in 2D

(b) downsampled map (for window size and stride both equal 2)

(c) generated waypoints in the downsampled map for $p = 25\%$

Figure 5.4: Downsampling and waypoint generation process for exploration.

5.5 Task assignment

The generated and filtered waypoints need to be assigned to individual UAVs. The assignment is solved by use of a clustering algorihm. Clustering belongs to the group of unsupervised machine learning methods. The goal of clustering is to partition the data into distinct groups (clusters), where data points within the same cluster are more similar to each other than to those in other clusters. The euclidean distance is the measure of similarity used in this scenario. The clustering algorithm of choice for the given task is **KMeans**, originally described in [35].

5.5.1 KMeans algorithm

The basic euclidean version of KMeans is defined as follows: Let's denote data points to be clustered as $\{\mathbf{w}_1, \mathbf{w}_2, \ldots, \mathbf{w}_n\}$. The task is to assign each of the data points into one of the k clusters, $\{C_1, C_2, \ldots, C_k\}$. Each cluster is represented by its centroid, $\mathbf{c}_1, \mathbf{c}_2, \ldots, \mathbf{c}_k$. The criterion function that should be minimized is then formulated as

$$J = \sum_{i=1}^{k} \sum_{\mathbf{w} \in C_i} \|\mathbf{w} - \mathbf{c}_i\|^2. \tag{5.3}$$

In other words, we want to find such clusters so that the sum of squared distances between data points and corresponding centroids of clusters will be minimal. **KMeans** is an iterative algorithm. In each iteration, it assigns each data point to the nearest centroid based on the euclidean distance. After all data points are assigned to clusters, the centroids are updated by calculating the mean of all data points in each cluster. These two steps are repeated until convergence. It is important to note that the outcome of the algorithm depends on the initialization of centroids and the method converges to local minima based on that initialization.

5.5.2 Constrained KMeans and initialization

For the purpose of assigning waypoints to the UAVs, the optimality of the solution is not required. However, we would like to assign waypoints to the UAV that are in its neighborhood. Moreover, we would like to guarantee that each UAV has at least one point assigned (the standard version of KMeans does not guarantee non-emptiness of the clusters). Therefore the constrained variant of KMeans [36] is used already implemented in `k-means-constrained`[1] python package. The centroids are initialized at the future positions of the UAVs. The minimum number of waypoints in each cluster is set to 2 (if the number of waypoints is sufficient).

5.6 Filtering recently visited waypoints

The following assumption is made: to acquire more measurements from different sides and localize the sources more precisely, it is better to keep the UAVs in motion rather than statically hover at certain position for longer time. Therefore are prioritized the waypoints that were not recently explored by any of the UAVs (meaning that no UAV was in a close proximity of the sensor in past seconds). For that purpose, we define short-term sensitivity vector $\hat{\mathbf{s}}$, which is independent of the sensitivity vector $\mathbf{s}$ defined in equation 4.7, although it is computed analogically.

Same as before, the vector $\hat{\mathbf{s}}^{[n=0]}$ is initialized with zeros. Lets denote $V^{[n:n+1]}$ the set of viewpoints that were newly sampled after update step n and needs to be processed. The short-term sensitivity vector $\hat{\mathbf{s}}^{[n+1]}$ with elements $\hat{s}_j^{[n+1]}$ is computed as:

$$\hat{s}_j^{[n+1]} = \alpha \hat{s}_j^{[n]} + \sum_{v \in V^{[n:n+1]}} s_{jv} \Delta_v. \tag{5.4}$$

We may notice that the only difference between short-term sensitivity equation 5.4 and sensitivity equation 4.7 is the scaling parameter $\alpha \in [0, 1)$. The forgetting factor α scales past $\hat{s}_j$ values with some non-negative < 1 number, making newly sampled and processed viewpoints more important. The α is a custom parameter to be set, the default value is $\alpha = 0.95$ (assuming the short-term sensitivity is updated every 2 seconds).

The filtering proceeds as follows:

$$W_{filtered} = \{w_x | \hat{s}_x \geq \underset{w_y \in W}{\text{median}}(\hat{s}_y)\}, \tag{5.5}$$

where W is the set of waypoints in the given cluster, w_x are waypoints with short-term sensitivity $\hat{s}$ higher or equal to median of short-term sensitivity of all waypoints in the cluster. Therefore half of the waypoints in the cluster that has been recently visited is removed in this step.

[1] Available at: https://pypi.org/project/k-means-constrained/

5.7 Sequence generation using TSP

After assigning all waypoints into clusters, the optimal sequence of waypoints inside the cluster should be determined. The proposed method is based on Travelling salesman problem (TSP).

5.7.1 Travelling salesman problem

The Travelling salesman problem (TSP) is a classical problem in computer science. From the computational complexity point of view, the TSP belongs to the class of NP-hard problems. The problem can be formulated as follows: A complete oriented graph is given, where V (set of vertices) represent locations that should be visited and E (set of edges) represents the distances between the vertices. The task is to find the path through the vertices (find a Hamiltonian cycle), so that each vertex is visited exactly once, the starting and ending point are the same and the distance of the path (the sum of weights assigned to the edges involved in the path) is minimal. The edges of the graph are typically stored in a distance matrix $\mathbf{D} \in \mathbb{R}^{|V|\times|V|}$, where $d_{ab} \in \mathbf{D}$ represents the distance from vertex a to vertex b.

5.7.2 Problem modifications

The problem of finding the optimal sequence of waypoints $\{v_1, v_2, \ldots, v_n\}$ for an UAV is transformed to the travelling salesman problem and solved using LKH solver[2]. However, we require some additional constraints, not only finding the minimal Hamiltonian cycle in the graph with respect to the euclidean distances between waypoints. The starting vertex of the sequence should be the future position of the drone denoted as vertex v_0. Secondly, the path of the UAV should not end in the starting vertex v_0, the last point of the sequence can be any of the waypoints $\{v_1, v_2, \ldots, v_n\}$. Because of that, we introduce dummy vertex denoted as v_F. We formulate the transformed problem as follows. The set of vertices of the graph is $\{v_0, v_1, v_2, \ldots, v_n, v_F\} \in V$, where:

- v_0 is the starting point of the optimal sequence of waypoints,
- $v_1, v_2, \ldots, v_n$ are the points to be visited by the UAV, and
- v_F is the dummy vertex that serves as the last point of any sequence found by the solver.

The distance matrix $\mathbf{D}$ of euclidean distances between each pair of $\{v_0, v_1, v_2, \ldots, v_n, v_F\}$

$$\mathbf{D}_{eukl} = \begin{pmatrix} 0 & d_{0,1} & d_{0,2} & \ldots & d_{0,n} & d_{1,F} \\ d_{1,0} & 0 & d_{1,2} & \ldots & d_{1,n} & d_{2,F} \\ d_{2,0} & d_{2,1} & 0 & \ldots & d_{2,n} & d_{3,F} \\ \ldots & \ldots & \ldots & \ldots & \ldots & \ldots \\ d_{n,0} & d_{n,1} & d_{n,2} & \ldots & 0 & d_{n,F} \\ d_{F,0} & d_{F,1} & d_{F,2} & \ldots & d_{F,n} & 0 \end{pmatrix} \tag{5.6}$$

is then modified in the following way: a positive constant M is introduced (it holds that $M > 10\max(d), \forall d \in \mathbf{D}_{eukl}$). The purpose of this constant is to forbid some edges in the graph so that they couldn't be chosen by the numerical solver. We set to M all edges that connects the dummy vertex v_F with all vertices $\{v_1, v_2, \ldots, v_n\}$, because we require the vertex v_F to be the last one in the optimal sequence. Additionally, the edge weight connecting the starting

[2]available at: http://webhotel4.ruc.dk/ keld/research/LKH/

point v_0 and v_F is also set to M. Furthermore, the distance from any vertex $\{v_1, v_2, \ldots, v_n\}$ to v_F is set to v_0, same as the vertex from v_F to v_0. The resulting modified distance matrix is

$$\mathbf{D_{mod}} = \begin{pmatrix} 0 & d_{0,1} & d_{0,2} & \ldots & d_{0,n} & M \\ M & 0 & d_{1,2} & \ldots & d_{1,n} & 0 \\ M & d_{2,1} & 0 & \ldots & d_{2,n} & 0 \\ \ldots & \ldots & \ldots & \ldots & \ldots & \ldots \\ M & d_{n,1} & d_{n,2} & \ldots & 0 & 0 \\ 0 & M & M & \ldots & M & 0 \end{pmatrix}. \tag{5.7}$$

Figure 5.5 illustrates the situation for 3 waypoints. The weights of the edges are painted in color. The back color represents the euklidean dstance between the point. The blue color represent edges whose value is set to 0. The weights of red edges are set to M.

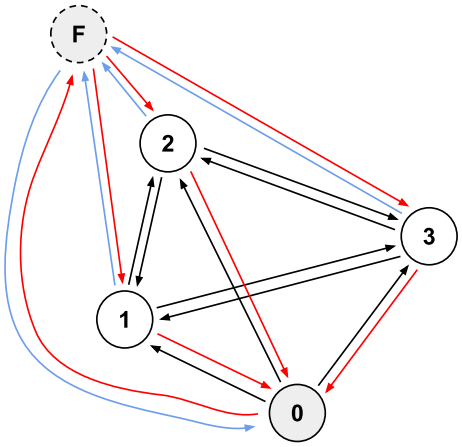

Figure 5.5: An illustration of the modified distance matrix $\mathbf{D}_{mod}$ for the TSP solver, that finds the optimal sequence of waypoints for each UAV. The vertex v_0 is the starting point of the sequence, vertices $\{v_1, v_2, v_3\}$ represent the waypoints to be visited by the UAV, v_F is an additional dummy virtual vertex. The black edges represent the euclidean distance between corresponding vertices, the value of red edges is set to positive constant M, the value of blue edges is set to 0.

5.8 Path planning

Once the sequence of waypoints for each UAV is determined, the last step is the path planning. The proposed multi-robot planner is based on the A* planning method implemented in the MRS UAV System [23]. The A* algorithm is a path-finding and graph traversal algorithm that solves the problem of finding the shortest path between two nodes in a graph. However, the paths should be collision-free, the minimal distance between each pair of UAVs should be above some safety threshold (4 m). Each UAV is assigned a certain priority and the paths are planned sequentially for each drone based on its priority. Once a path for a drone is generated, the inflated (by the safety distance radius $r = 4$ m) points of the path are considered as obstacles for all drones with the lower priority. If any of the waypoints is not reachable (for example some drone with higher priority planned path in close distance to it), the waypoint is skipped. The path is then smoothed by the MRS UAV system [23] onboard

the drone and executed by the drone's controller. The proposed planning method is described in Figure 5.6.

```
function PLAN_PATHS(drones_waypoints, drones_poses)
    planned_paths ← {}
    for drone ∈ drones do                          ▷ iterate over drones based on priority
        obstacles ← {}
        for path ∈ planned_paths do
            obstacles ← obstacles ∪ INFLATE_POINTS(path)
        end for
        path ← {}
        segment_start ← drone_pose
        for waypoint ∈ drone_waypoints do
            if waypoint ∈ obstacles then
                continue
            end if
            path_segment ← ASTAR_PLANNER(start, waypoint, obstacles)
            segment_start ← waypoint
            path ← path ∪ path_segment
        end for
        planned_paths ← planned_paths ∪ path
    end for
    return planned_paths
end function
```

Figure 5.6: Multi-path planning procedure. Each drone is processed sequentially based on its priority. The points belonging to the already planned paths (for drones with higher priority) are inflated and treated as obstacles. The A* method is used to find shortest path between the consecutive waypoints. The waypoint is skipped if not reachable.

Chapter 6

Results

This chapter demonstrates the functionality of the proposed method[1] for the localization of sources of ionizing radiation and its individual components. Unfortunately, it was not possible to test the proposed methods using real sources of ionizing radiation for organizational reasons, since the use of radioactive materials is strictly regulated and requires coordination with state authorities (National Institute for Nuclear, Chemical and Biological Protection) and manufacturer of the MiniPIX3. Another problem is the absence of methods for comparison, that would be a) available, b) capable of localization of multiple sources using the Compton camera measurements. Therefore we use the back-projection reconstruction method (described in Chapter 3) as a baseline. This chapter presents results of the Monte Carlo simulation (Section 6.1), performance of the system on recorded real-world data (Section 6.2), in simulation (Section 6.3) and in real-world experiment with simulated data (Section 6.4).

6.1 Monte Carlo simulation of the sensor's sensitivity

The assessment of the directional sensitivity of the MiniPIX3 sensor was carried out using the Monte Carlo simulation described in Chapter 4. Each omnidirectional simulated source (located 1 m from the sensor) emitted 10^{10} 662 keV photons from each position. Shortly speaking, the simulator recorded the number of photons that a) reached the sensor's surface (more precisely, the CdTe block, where the ionizing particles interact with CdTe material) and b) undergone the interactions (Compton scattering, photoelectric absorption) leading to the Compton cone detection. Results of the Monte Carlo simulations are shown in Figure 6.1. The corresponding geometry of the CdTe block is shown in 6.1b.

The MiniPIX3 sensor's directional sensitivity is depicted in 6.1a. It can be observed that the probability of a particle being detected as a Compton event is nearly the same from all directions (more precisely, it varies from 3.79×10^{-8} to 5.15×10^{-8}). The probability of reaching the sensor's surface (given the solid angle of the sensor from different positions) is shown in 6.1c. A particle emitted in front of the sensor (along the x-axis) is more likely to hit the CdTe block than another one emitted from the side (y-axis and z-axis), where the visible surface of the CdTe block is the smallest. On the other hand, the probability of Compton scattering as well as photoelectric absorption (that together lead to the detection of a Compton cone) depend on the trajectory of the incident and scattered photon. The longer the intersection of an ionizing particle and the CdTe block is, the more likely the interactions happen. Therefore a photon reaching the sensor's surface from the side more likely causes the Compton measurement, as can be seen in 6.1d. In summary, both effects (probability of reaching the CdTe block and probability of necessary interactions) neglect each other and lead to the almost uniform directional sensitivity of the MiniPIX3 sensor.

[1] Videos from the experiments are available here: `http://mrs.felk.cvut.cz/theses/werner2023thesis`

The absolute values of estimated probabilities and also worth mentioning. The MiniPIX3 sensor with its dimensions $14.08 \times 14.08 \times 2$ mm is very small compared to the distance between the UAV carrying the sensor and sources of ionizing radiation. Moreover, approximately only 1 of 100 662 keV photons that reach the MiniPIX3 sensor can be detected in the Compton camera mode. For illustration: based on the simulation results, only ≈ 15 Compton events can be possibly detected (on average) by a MiniPIX3 sensor located 5 m from a source of 662 keV photons with activity 1 GBq (assuming exposure time 10 s). This estimate can be seen as an upper bound since it does not take into account other aspects of the detection process. For example, other interactions might occur (the incident photon might be immediately absorbed without any Compton scattering), and the detection process might not estimate all the Compton cones correctly due to the noise caused by other particles detected by the Timepix detector at the same time.

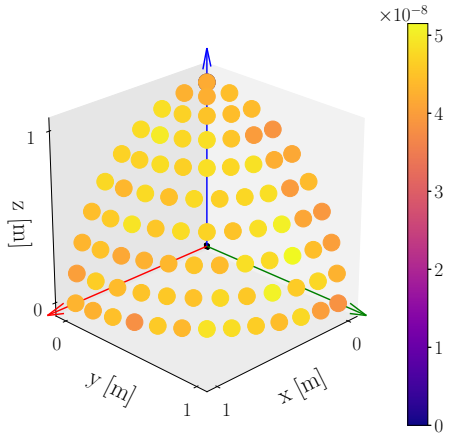

(a) p(cone detected)

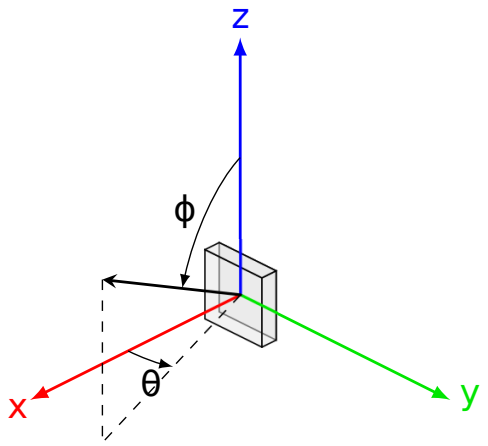

(b) MiniPIX3 sensor geometry. The CdTe block (grey) has dimensions 14.08 × 14.08 × 2 mm

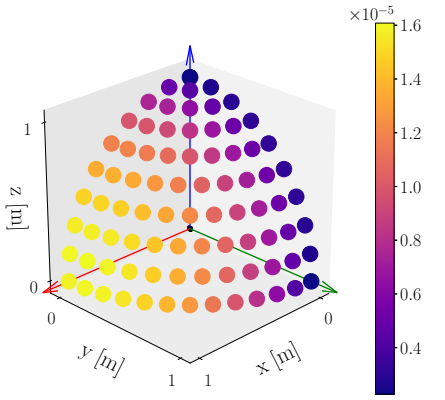

(c) p(reaching the sensor)

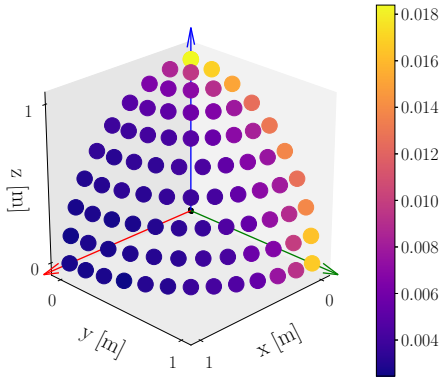

(d) p(cone detected | reaching the sensor)

Figure 6.1: Direction sensitivity of the MiniPIX3 sensor (geometry of the sensor depicted in (b)). The probability that a 662 keV photon emitted at the corresponding position causes a Compton cone is depicted in (a). The probability that the particle emitted at a given position reaches the detector is depicted in (c). Lastly, the probability that a photon (that reached the sensor) causes a Compton cone is illustrated in (d).

6.2 Evaluation of MLEM method based on real-world data

The proposed MLEM method for radiation mapping has been tested using data from real-world experiments that were carried out in September 2022 (before the work on this thesis started). Although the pre-recorded real-world data were collected in realistic conditions with real sensors and sources of ionizing radiation, the prerecorded data do not allow to fully test capabilities of the proposed system. The reason is the strong dependency between drones trajectories during the experiment and recorded measurements (caused by properties of the ionizing radiation, such as the inverse square law, that is significantly reducing distance from which a radioactive source might be perceived). Therefore the outcome of reconstruction strongly depends on in which areas the drones flew during the recorded experiments.

6.2.1 Setup and course of the experiment (data collection)

The area of interest of size $\approx 40 \times 30$ m was scanned by a group of four UAVs equipped with MiniPIX3 sensor. The UAVs were localized using Global Positioning System (GPS). The drones were controlled by the method proposed in [2]. In the beginning of the experiment, the drones were following a predefined trajectory covering the whole area of interest uniformly. After the first 8 Compton cones were detected, three drones were flying 3 m above the ground encircling the current single-hypothesis estimate of the source position (filtered by a LKF). The last drone with flight height 6 m was following a predefined path covering the whole area. Four sources of Cesium-137 with activity $1900, 500, 180, 50$ MBq were located at positions shown in 6.2b. During the run of the experiment, the drones were mostly encircling the 500 MBq source position. The fourth UAV flying 6 m above the ground twice detected photons originating from the 1900 MBq source. As a consequence, the single hypothesis moved towards the strongest source. However, the group of UAVs moved back to the 500 MBq source after a while. The whole experiment took ≈ 10 min, and 263 Compton cones were recorded.

6.2.2 Evaluation of the MLEM method

The results of the proposed MLEM estimation method are presented in Figure 6.2. The area of interest was discretized with 1 m resolution, and the number of iterations of the MLEM method was set to 10. The viewpoints (positions of the drones) were sampled with 5 Hz, and the MLEM estimate was updated every 2 s. The uncertainty of the cone angle The final estimate of the emission intensity $\boldsymbol{\lambda}$ (based on all data acquired during the experiment) is presented in 6.2a. The sensitivity of detection (6.2d) confirms what was stated before - the drones were mostly encircling the 500 MBq source at position $(-2, -10)$, which was also correctly localized. The area in the vicinity of the 1900 MBq source at position $(16, 0)$ was much less explored by the UAVs (and therefore fewer Compton cones originating there were recorded). Despite the much lower sensitivity in that area, the MLEM method estimated some local maxima in the neighbourhood of the true position of the strongest source. The two weakest sources of radiation are indistinguishable from the noise.

6.2.3 Summary

The results of the MLEM reconstruction are heavily affected by a noise in measurements. First of all, the UAVs were localized using GPS method that might be effected by a position

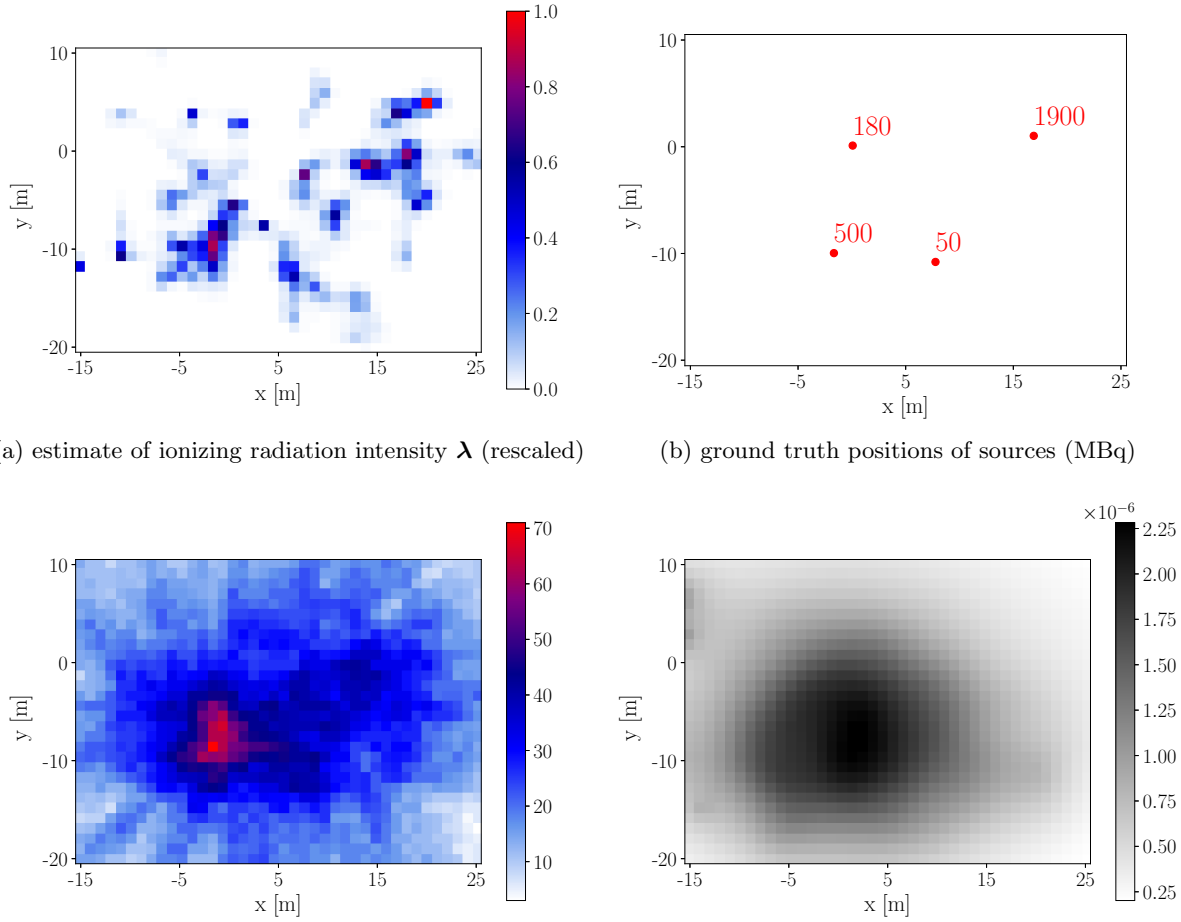

(a) estimate of ionizing radiation intensity $\boldsymbol{\lambda}$ (rescaled)

(b) ground truth positions of sources (MBq)

(c) back-projection (number of Compton cones)

(d) sensitivity of detection $\mathbf{s}$

Figure 6.2: The MLEM method evaluated on pre-recorded real-world data.

error of several meters. The position error propagates to the uncertainty of the Compton cone origins. Furthermore, the real MiniPIX3 sensors produced many outliers — e.g. Compton cones pointing upwards or not intersecting any source position. The noisy measurements are probably caused by the working principle of an unshielded single-layer Compton camera, where ionizing particles coming from different directions might affect the Cone reconstruction procedure. This might be a limiting factor for the localization of multiple sources of ionizing radiation (with high emission activity) that are close to each other. The single-layer Compton camera is able to estimate the direction of incoming ionizing photons only if the number of interactions detected by the Timepix3 pixel detector inside the MiniPIX3 sensor is relatively low and corresponding interactions can be paired together correctly. However, the presence of multiple sources in close vicinity increases the particle flux and may potentially increase the number of outliers.

In summary, the comparison of MLEM estimate (6.2a) and back-projection (6.2c) show that the MLEM significantly improved the reconstruction quality. The 1900 MBq source was localized (despite the low number of recorded photons originating there) thanks to the weighting of the estimate with the sensitivity of detection in the MLEM algorithm. Better results might be achieved by using an active search strategy, where the drones are controlled

in order to improve the quality of the current MLEM estimate.

6.3 Evaluation of MLEM and search strategy in simulation

The MLEM estimation method has been tested together with the proposed search strategy in *Gazebo* simulator. The results were compared with the back-projection method, that served as a baseline.

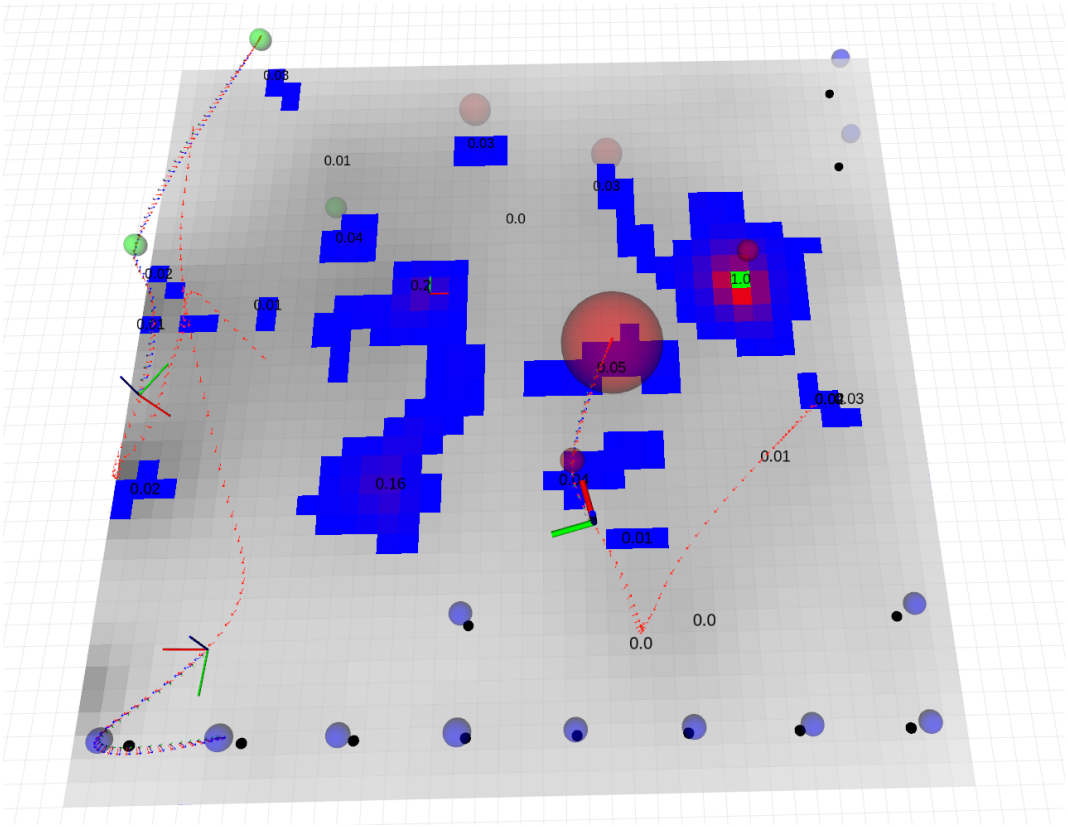

Figure 6.3: Experiments in *Gazebo* simulator. The UAVs are autonomously mapping sources of ionizing radiation place in the area 40×40 m (resolution $r = 1$ m). The current MLEM estimate is visualized using blue-red-green distribution and black numbers denoting the relative activity of local maxima at the given position. The drones follow the trajectories (red arrows) to visit waypoints (depicted as transparent spheres). Two drones are designated for exploitation (red and green waypoints) and one for exploration (blue waypoints).

6.3.1 Simulated experiment 1

The distribution and activity of the radioactive sources were the same as in the real-world experiments described in the previous section. Three drones flying 3 m above the ground were used during the experiment. The simulation process (visualized in *RViz*) is shown in Figure 6.3. Two drones were designated for exploitation (visiting the positions where the sources of radiation are present based on the latest MLEM estimate), and one for exploration (visiting positions with the lowest sensitivity). The drones were initialized at positions $(-15, -10)$,

$(-5, -10)$ and $(5, -10)$ and controlled by the proposed search strategy in the rest of the experiment.

Measurement noise

Extra noise was added to the measurements to model the real-world conditions. The inaccuracy in the drone position (resulting in the shifted origin of the Compton cone) was modelled with the Normal distribution $\mathcal{N}(\mu_{pos}, \sigma_{pos})$ with zero means $\mu_{pos} = 0$ and standard deviation $\sigma_{pos} = 1.5\,\text{m}$. The noise in energy measurements of the simulated MiniPIX3 sensor was modeled the Normal distribution $\mathcal{N}(\mu_{energy}, \sigma_{energy})$ with zero mean $\mu_{energy} = 0$ and standard deviation $\sigma_{energy} = 7\,\text{keV}$.

Results

The results of the MLEM reconstruction are presented in Figure 6.4. The progress of radiation mapping is illustrated in 6.4a (time $t = 25\,\text{s}$) and 6.4c ($t = 100\,\text{s}$), corresponding sensitivity of detection is presented in 6.4b, 6.4d. The active search strategy controlled the drones in order to acquire more measurements, which significantly improved the initial inaccurate estimate (based on a smaller number of Compton cones). We may notice that after 100 s of flight the UAVs correctly localized the 1900 MBq , 500 MBq and 280 MBq sources of simulated ionizing radiation. The 50 MBq source was not recognized due to its low emission activity or because it was filtered out during the later iterations of the MLEM algorithm. The MLEM method significantly improved the solution compared to the back-projection illustrated in 6.4e.

Summary

Three sources with the highest emission activity were correctly localized in less than 100 s. The proposed MLEM estimation method, together with the autonomous search strategy, worked as intended. Although the MLEM method does not estimate the positions of sources perfectly for a small number of measurements, the active search strategy guides the UAVs in order to acquire more measurements, which further improves the estimate's quality. The extensive testing in simulations showed that the inaccuracy in the origins of the Compton cones significantly reduces the quality of reconstruction, which highlights the need for accurate localization of drones during real-world experiments. In summary, the experiment showed that the proposed method is capable of autonomous localization of multiple sources of ionizing radiation (of different emission activity).

Simulation vs. reality

The simulated noise in the drone's position and energies helped to bring the simulation closer to real-world conditions. However, the used simulator of ionizing radiation simulates each source-sensor pair independently, which ignores the fact that ionizing particles from multiple sources might interact in the sensor at the same time (causing outliers), therefore the simulation is not as accurate as it could be. Improving the simulator in order to process interactions caused by different sources simultaneously presents a possible direction for future research.

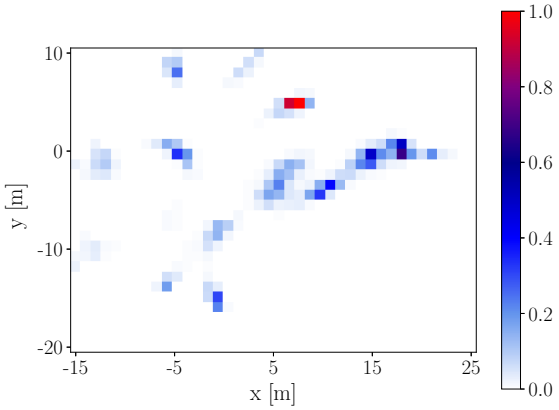

(a) ($t = 25\,\mathrm{s}$) source intensities $\boldsymbol{\lambda}$ (rescaled)

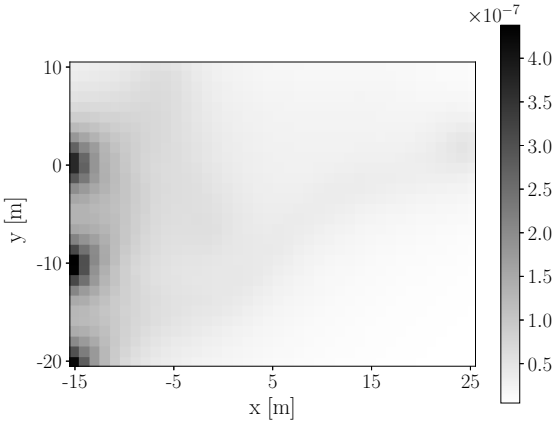

(b) ($t = 25\,\mathrm{s}$) sensitivity of detection $\mathbf{s}$

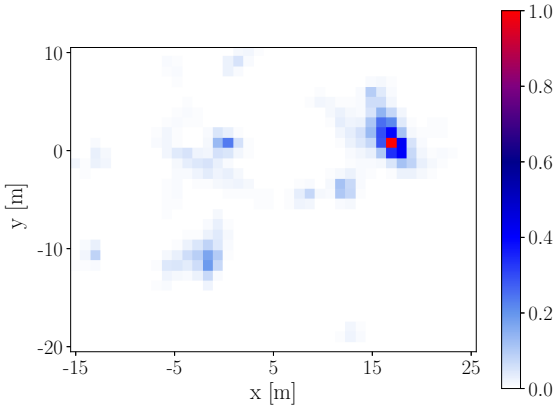

(c) ($t = 100\,\mathrm{s}$) source intensities $\boldsymbol{\lambda}$ (rescaled)

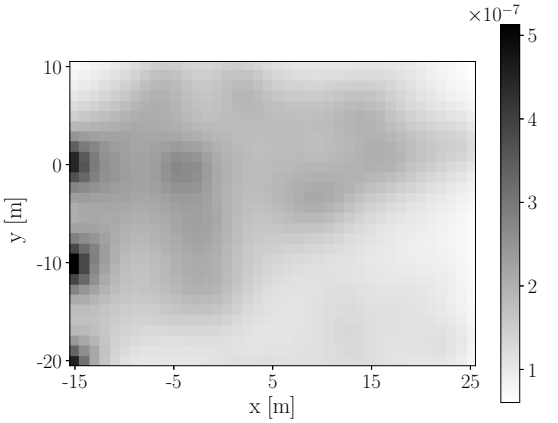

(d) ($t = 100\,\mathrm{s}$) sensitivity of detection $\mathbf{s}$

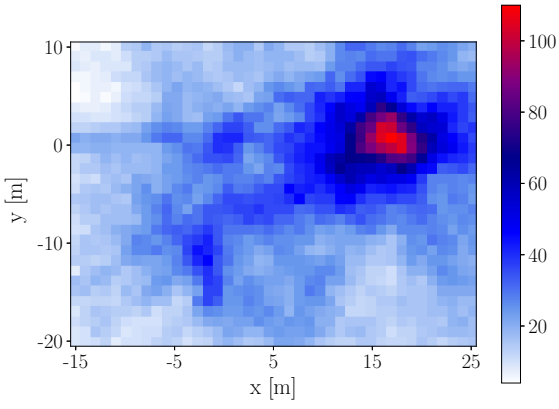

(e) ($t = 100\,\mathrm{s}$) back projection (number of cones)

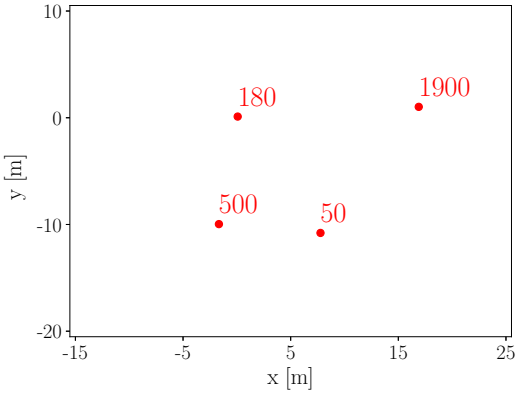

(f) ground truth positions of sources (MBq)

Figure 6.4: Results of the experiment with three UAVs and four sources of ionizing radiation simulated in *Gazebo*. The progress of the MLEM reconstruction method is shown in (a), (b) and (c), (d). The back-projection of all cones measured in the first 100 s is shown in (e).

6.3.2 Simulated experiment 2

The ability to map multiple sources of ionizing radiation is demonstrated on the following simulated scenario: the size of the area, number of drones, simulated noise and other parameters remain the same as in the previous experiment. Only the activity of sources is set to the same value for convenience. The source is considered as detected if the estimated emission activity ($\boldsymbol{\lambda}$ rescaled to $0-1$ range) at the ground-truth source position exceeds detection threshold 0.5 (in the vicinity of 2 m around the ground-truth position) and remains above threshold 0.3 during the rest of the experiment. Since the radiation emission is a stochastic process, the same instance was repeated multiple times. Results are presented in Figure 6.5.

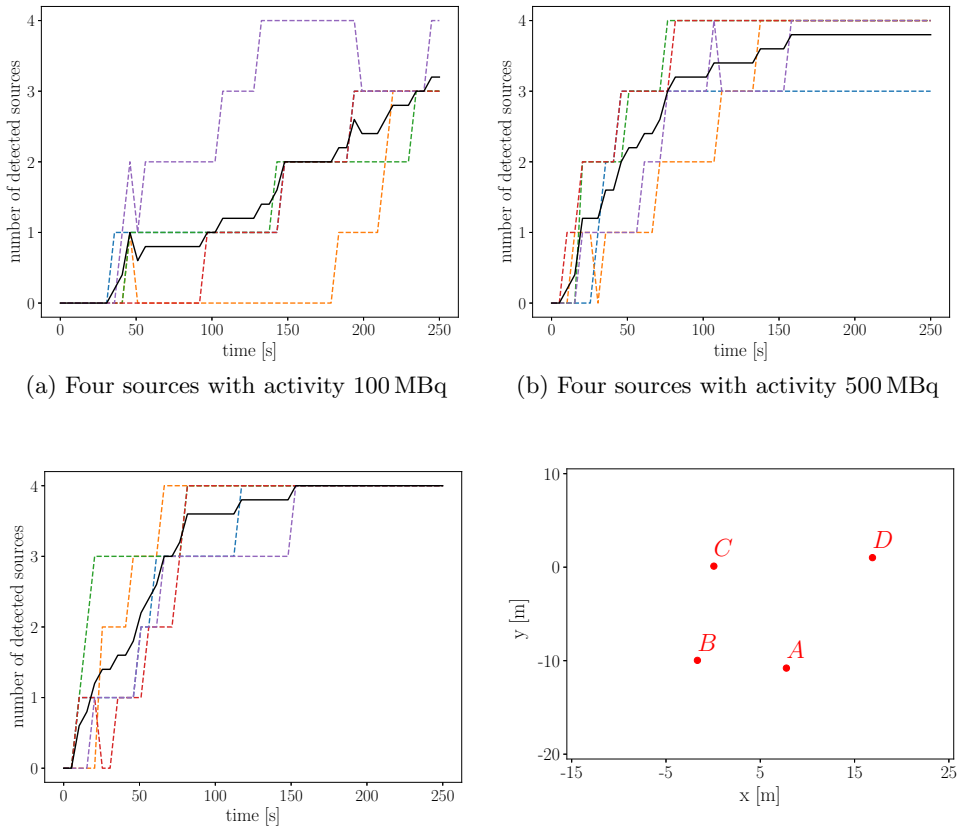

(a) Four sources with activity 100 MBq

(b) Four sources with activity 500 MBq

(c) Four sources with activity 2000 MBq

(d) Ground truth positions

Figure 6.5: The number of correctly detected sources with the same emission activity (located at positions (d)). Dashed lines represent the individual experiments (each scenario was repeated 5 times), the black line is the average. The detection was evaluated every 5 seconds.

Results

We can see that the low emission activity of the sources prolongs the detection time (6.5a), however, the method was still able to localize positions of the three sources (on average) in less than 250 s. The method was able to correctly localize four 2000 MBq sources is less than 170 s in all scenarios. We may notice that the number of detected sources also sometimes decreased during the time (see the purple line in 6.5c). This shows that the method do

not perfectly estimate the relative emission activity of the sources, which is caused by the stochastic nature of radioactive decay and limited number of measurements.

6.4 Real-world experiment with simulated radiation

The proposed search strategy has been tested using real UAVs during the field experiments. Since the real sources of radiation were not available, the ionizing radiation was simulated onboard each UAV. The main purpose of the experiment was to test the search strategy with real hardware and gain some experience with real-world conditions, where many things are not as simple as in simulation.

(a) The DJI f450 drones used during the experiments. (b) The area of interest and UAVs searching for the (simulated) sources of ionizing radiation.

Figure 6.6: Field experiments with real hardware. The drones (a) were mapping the simulated radioactive sources located somewhere in the open field (b).

6.4.1 Experiment setup

The size of the explored area was 100×100 m, the resolution of each map cell was set to 0.5 m. The simulator of ionizing radiation was running onboard each UAV, simulating the radiation coming from sources at predefined positions. The UAVs were localized using GPS. However, the noise in GPS position measurement did not affect the simulated radiation data since the drones used their belief (not the real position) when simulating incoming ionizing photons. The viewpoints (positions of the drones) were sampled with 5 Hz, and the MLEM estimate was updated every 2 s. Four simulated sources of 662 keV photons with activity $2000, 1000, 1000, 500$ MBq were located at positions shown in 6.7e.

6.4.2 Results

In the initial phase (from time $t = 0$ min to time $t = 2$ min), the drones flew over the area once in a "zig-zag" pattern following the predefined trajectory (covering the area uniformly, as can be seen in 6.7b) and measured first 17 Compton cones. The "zig-zag" trajectory was precomputed using the MRS UAV System [23]. The MLEM estimate and sensitivity of

detection after the initial phase is shown in 6.7a and 6.7b. Then (at the time $t = 2\,\text{min}$), the proposed search strategy took control—two drones were designated for exploitation, one for exploration. The trajectories of the UAVs during the search phase (6.7f) show that the two "exploitation" drones focused on acquiring more measurements while the third drone was exploring the unexplored area. The final estimate of radiation sources intensities (at the end of the experiment $t = 10\,\text{min}$) is shown in 6.7c. Three of four sources of simulated ionizing radiation were correctly localized (together with their relative emission activity, which is shown in table Table 6.1). The weakest 500 MBq source at position $(75, 75)$ was not discovered despite the fact that the exploration drone flew around it multiple times (see blue path in 6.7f). The minimum distance between the UAVs was not below the safety threshold (4 m) during the whole flight, therefore all the planned trajectories were non-colliding. 267 Compton events were recorded during the whole experiment.

Sources		relative activity	
position	activity	ground truth	MLEM estimate
(10, 20)	2000 MBq	1.0	**1.0**
(20, 20)	1000 MBq	0.5	**0.49**
(80, 80)	1000 MBq	0.5	**0.52**
(75, 75)	500 MBq	0.25	**0.0**

Table 6.1: Results of the real-world experiment with simulated data. The last column presents estimated relative activity at the map positions that correspond to the ground truth position of the given source.

6.4.3 Summary

The experiment proved that the whole system be used for fast radiation mapping in large open areas and perform all the computations in real-time. The proposed search strategy, together with the MLEM mapping method, worked as intended. The initial estimate of source positions was significantly improved during the search phase. Although the maximum likelihood does not provide an accurate estimate for a small number of cones (see MLEM estimate in 6.7a generated from 17 Compton cones), the inaccurate estimate "attracts" the UAVs that come closer and likely measure more ionizing photons, that guide the UAVs to the actual position of the source. This shows that online estimation (together with an active search strategy) is beneficial for the autonomous detection of ionizing radiation.

Three of four sources of simulated radiation were localized during the experiment. The weakest 500 MBq was not discovered during the flight, which is probably caused more by the limited sensitivity of the (simulated) MiniPIX3 sensor than by the estimation method. It is important to note that the simulated radiation data were generated in ideal conditions, without any noise in the drone position, energies measured in the sensor or particles causing false positive Compton detections. Therefore the results of MLEM reconstruction results are more accurate compared to the previously described experiments with real sources of ionizing radiation.

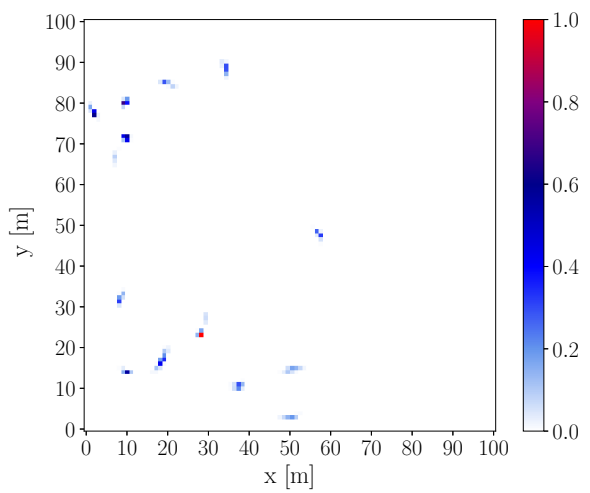

(a) source intensities $\boldsymbol{\lambda}$ after the initial phase ($t = 2\,\text{min}$)

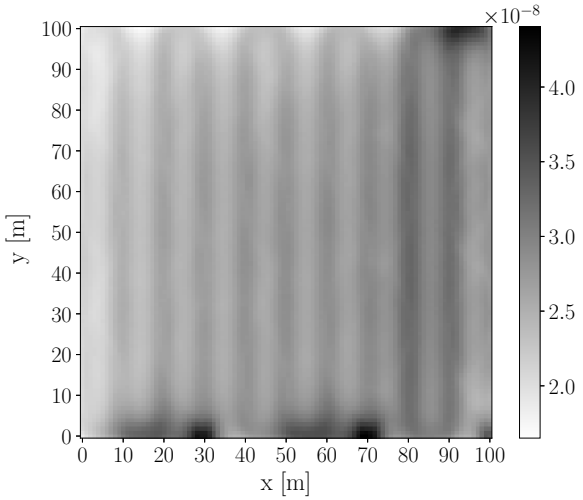

(b) Sensitivity $\mathbf{s}$ after the initial phase ($t = 2\,\text{min}$)

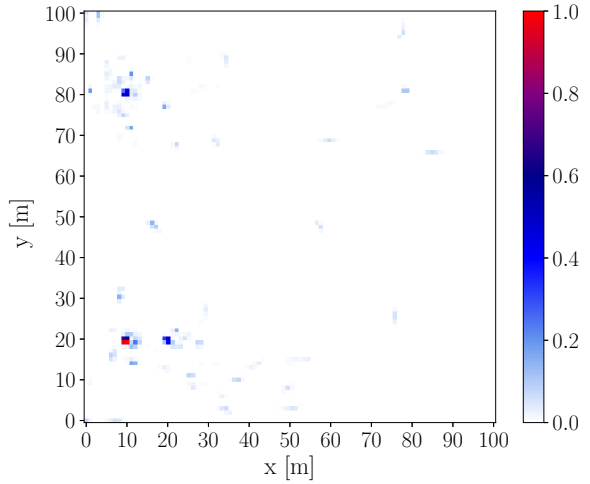

(c) final estimate of source intensities $\boldsymbol{\lambda}(t = 10\,\text{min})$

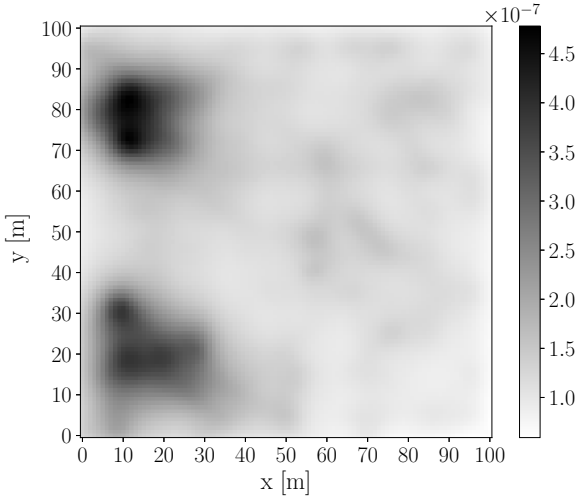

(d) Sensitivity $\mathbf{s}$ at the end of the experiment ($t = 10\,\text{min}$)

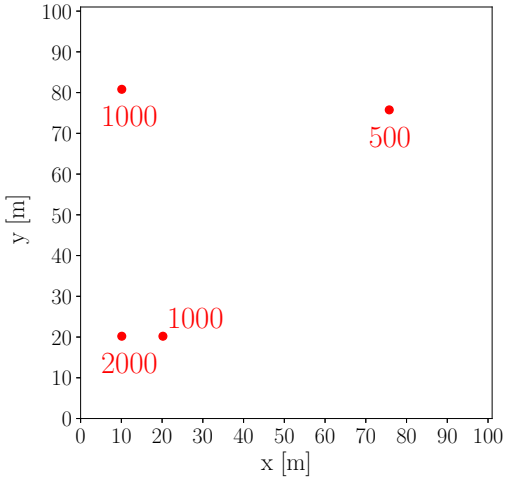

(e) ground truth (MBq)

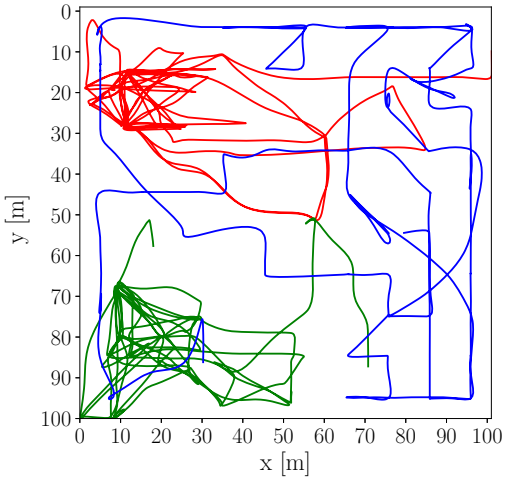

(f) Paths of UAVs during the search phase (red, green — exploitation, blue — exploration)

Figure 6.7: Real-world experiments with simulated data. The MLEM estimate, sensitivity and drone paths during and after the experiment ($t = 2\,\text{min}$, $t = 10\,\text{min}$) are presented.

Chapter 7

Conclusion

The goal of this thesis was to research, design, and implement an algorithm and software method for collaborative sensor fusion of measured ionizing radiation data from a group of UAVs. The presented solution based on the MLEM algorithm is able to localize multiple sources of ionizing radiation based on data acquired by a group of drones equipped with a miniature Compton camera. All the subtasks in the thesis assignment were fulfilled:

- The author of the thesis familiarized himself with the MRS UAV System and the principles of the Compton camera detector. The use of MRS UAV System was demonstrated during simulated and real-world experiments described in Chapter 6. An overview of the principles of the Compton camera is presented in Chapter 2.
- A method for the localization of multiple sources of ionizing radiation using the Compton camera measurements was implemented. The online estimation method is based on the MLEM algorithm, which was adapted to the proposed application. The directional sensitivity of the MiniPIX3 sensor was studied using Monte Carlo simulation. The proposed method takes into account the sensitivity of detection (how likely a potential source at a certain position has been detected by the UAVs during the flight), which improves the quality of estimate in scenarios with multiple sources of radiation with different emission activity. The proposed localization method is presented in Chapter 4.
- The proposed active search strategy for a small group of UAV is presented in Chapter 5. The centralized search strategy takes the current estimate of radioactive sources as an input and generates waypoints for the UAVs in order to acquire more measurements and explore less explored parts of the area. The generated waypoints are assigned to the individual drones, and a non-colliding path connecting the waypoints is computed for each drone.
- The proposed estimation method and the search strategy were evaluated on recorded real-world data and in simulation, as presented in Chapter 6. The functionality of the whole system was also demonstrated during outdoor experiments with real hardware and simulated sources of radiation (in addition to the scope of the thesis assignment).

7.1 Discussion

In summary, the proposed method for radiation mapping, in combination with the active search strategy, seems to be applicable for the task of localization of multiple sources of ionizing radiation. However, this result is based mostly on simulations since it was not possible to test the proposed method with real sources of radiation. Further testing in simulations and with real-world sources of ionizing radiation is needed in the future. Let us summarize the properties of the proposed solution and its limitations.

Many limiting factors originate in the nature of the MiniPIX3 sensor, Compton measurements and properties of ionizing radiation. The biggest issue is the limited number of data

that is given by the relatively low sensitivity of the MiniPIX3 sensor. The limited sensitivity is given by the fact that the sensor is very small and that only less than $\approx 1\%$ of gamma photons (based on the Monte Carlo simulation) reaching the semiconductor CdTe detection block cause the Compton event. Therefore less active sources (with emission activity of tens of MBq and less) might not be easily detected by the proposed multi-robot system (more precisely, their detection requires longer time spend in the vicinity of the source). The working principle of the single-layer Compton camera (where the corresponding interactions are paired together based on their times of arrival) also limits the sensitivity of the MiniPIX3 sensor (working as the Compton camera) in scenarios with high emission activity of radioactive sources. If the number of interactions inside the CdTe semiconductor block is too high, the sensor can no longer correctly deduce which interactions should be paired together, and the number of outliers increases (this is more a speculation based on the author's understanding of the sensors working principle, since the recorded data did not contain scenarios of sources with activity higher than 2 GBq and the simulator cannot properly model this effect). The effect of the very active sources on the detection capability of the MiniPIX3 sensor needs to be investigated. However, we can conclude that the proposed method is suitable for the detection of sources with mid-level emission activity and cannot detect sources with very low or high activity).

Another limitation is that the output of the proposed MLEM method does not provide accurate absolute information about the emission activity of the source. Although the optimized hidden parameters $\boldsymbol{\lambda}$ have meaning of expected emission rate, it turned out that the number of measured Compton cones ($\approx 10^2 - 10^3$) during recorded real-world experiments was not sufficient to accurately model the absolute emission activity of the source and the output of the MLEM method can serve only as information about the relative emission activity of the sources present in the area. Another problem is that the MLEM method does not provide any guarantees on the quality of the estimate. Therefore the method can be used for fast and inaccurate detection of possible radioactive hot spots in unknown areas (and the estimated source needs to be further verified by other types of sensors that can accurately estimate the activity of the detected source).

Unlike the solution described in [2] for single-source localization using LKF, the proposed method can't localize the moving source of ionizing radiation. The solution proposed in [2] based on LKF is better suited for scenarios with single source and very low number of measurements (≈ 10). The maximum likelihood method generally requires more data to produce accurate estimates of the underlying probability distribution, which is partially compensated by the active search strategy.

7.2 Future work

The experiments with recorded real-world data showed that the real measurements acquired by the MiniPIX3 sensor contain many outliers and noise in the measurements that significantly affected the quality of MLEM reconstruction. Experiments in simulation (with simulated noise) showed that the proposed active search strategy is able to overcome the noise in measurements by controlling the drones to get more data. However, the combination of the proposed search strategy and the MLEM estimation method could not be tested with real sources of ionizing radiation (due to organizational reasons). Future testing with real Cesium-137 sources is therefore needed for accurate evaluation. Further investigation of parameters influencing the quality and speed of reconstruction (noise, size of the area, number of sources and their activity, number of drones) also presents a task for future.

Another possible improvement of the proposed method is optimal planning and task allocation during the search strategy. More advanced state-of-the-art methods can be applied, such as solving multi-robot Orienteering problem when planning the future movement of the drones, better task allocation methods or coverage path planning for the exploration. In general, the search strategy can be optimized by applying some global planning methods.

The proposed localization method was developed for 2D radiation mapping in an outdoor open area. A possible future extension is to fuse the Compton measurements with a 3D map of the environment (computed by some SLAM method based on LiDAR data). The set of obstacles generated by the SLAM method can be used as a set of possible source locations in the MLEM algorithm. This would open the possibility of monitoring radiation even in areas with obstacles or in the indoor environment. Fusion of the direction-based Compton camera sensor with some intensity based detectors might help to estimate not only the realitve, but also absolute emission activity of the source.

Chapter 8

References

[1] A. H. Compton, "A Quantum Theory of the Scattering of X-rays by Light Elements," *Phys. Rev.*, vol. 21, pp. 483–502, 5 May 1923.

[2] T. Baca, P. Stibinger, D. Doubravova, D. Turecek, J. Solc, J. Rusnak, M. Saska, and J. Jakubek, "Gamma Radiation Source Localization for Micro Aerial Vehicles with a Miniature Single-Detector Compton Event Camera," in *2021 International Conference on Unmanned Aircraft Systems (ICUAS)*, IEEE, Jun. 2021, pp. 338–346.

[3] L. Marques, A. Vale, and P. Vaz, "State-of-the-Art Mobile Radiation Detection Systems for Different Scenarios," *Sensors*, vol. 21, no. 4, 2021.

[4] K. Nagatani, S. Kiribayashi, Y. Okada, K. Otake, K. Yoshida, S. Tadokoro, T. Nishimura, T. Yoshida, E. Koyanagi, M. Fukushima, and S. Kawatsuma, "Emergency response to the nuclear accident at the fukushima daiichi nuclear power plants using mobile rescue robots," en, *Journal of Field Robotics*, vol. 30, no. 1, 44–63, Oct. 2012.

[5] Y. Sato, Y. Terasaka, W. Utsugi, H. Kikuchi, H. Kiyooka, and T. Torii, "Radiation imaging using a compact Compton camera mounted on a crawler robot inside reactor buildings of Fukushima Daiichi Nuclear Power Station," *Journal of Nuclear Science and Technology*, vol. 56, no. 9-10, pp. 801–808, 2019.

[6] Y. Sanada and T. Torii, "Aerial radiation monitoring around the Fukushima Dai-ichi nuclear power plant using an unmanned helicopter," *Journal of Environmental Radioactivity*, vol. 139, pp. 294–299, Jan. 2015.

[7] J. Towler, B. Krawiec, and K. Kochersberger, "Radiation Mapping in Post-Disaster Environments Using an Autonomous Helicopter," *Remote Sensing*, vol. 4, no. 7, pp. 1995–2015, Jul. 2012.

[8] J. Jiang, K. Shimazoe, Y. Nakamura, H. Takahashi, Y. Shikaze, Y. Nishizawa, M. Yoshida, Y. Sanada, T. Torii, M. Yoshino, S. Ito, T. Endo, K. Tsutsumi, S. Kato, H. Sato, Y. Usuki, S. Kurosawa, K. Kamada, and A. Yoshikawa, "A prototype of aerial radiation monitoring system using an unmanned helicopter mounting a GAGG scintillator Compton camera," *Journal of Nuclear Science and Technology*, vol. 53, no. 7, pp. 1067–1075, Oct. 2015.

[9] S. Mochizuki, J. Kataoka, L. Tagawa, Y. Iwamoto, H. Okochi, N. Katsumi, S. Kinno, M. Arimoto, T. Maruhashi, K. Fujieda, T. Kurihara, and S. Ohsuka, "First demonstration of aerial gamma-ray imaging using drone for prompt radiation survey in Fukushima," *Journal of Instrumentation*, vol. 12, no. 11, P11014, Nov. 2017.

[10] Y. Sato, S. Ozawa, Y. Terasaka, M. Kaburagi, Y. Tanifuji, K. Kawabata, H. N. Miyamura, R. Izumi, T. Suzuki, and T. Torii, "Remote radiation imaging system using a compact gamma-ray imager mounted on a multicopter drone," *Journal of Nuclear Science and Technology*, vol. 55, no. 1, pp. 90–96, 2018.

[11] J. MacFarlane, O. Payton, A. Keatley, G. Scott, H. Pullin, R. Crane, M. Smilion, I. Popescu, V. Curlea, and T. Scott, "Lightweight aerial vehicles for monitoring, assessment and mapping of radiation anomalies," *Journal of Environmental Radioactivity*, vol. 136, pp. 127–130, Oct. 2014.

[12] G. Christie, A. Shoemaker, K. Kochersberger, P. Tokekar, L. McLean, and A. Leonessa, "Radiation search operations using scene understanding with autonomous UAV and UGV," *Journal of Field Robotics*, vol. 34, no. 8, pp. 1450–1468, May 2017.

[13] P. Martin, S. Kwong, N. Smith, Y. Yamashiki, O. Payton, F. Russell-Pavier, J. Fardoulis, D. Richards, and T. Scott, "3D unmanned aerial vehicle radiation mapping for assessing contaminant distribution and mobility," *International Journal of Applied Earth Observation and Geoinformation*, vol. 52, pp. 12–19, Oct. 2016.

[14] F. Mascarich, M. Kulkarni, P. De Petris, T. Wilson, and K. Alexis, "Autonomous mapping and spectroscopic analysis of distributed radiation fields using aerial robots," *Autonomous Robots*, vol. 47, pp. 1–22, Nov. 2022, ISSN: 1573-7527.

[15] P. Štibinger, T. Báča, and M. Saska, "Localization of Ionizing Radiation Sources by Cooperating Micro Aerial Vehicles With Pixel Detectors in Real-Time," *IEEE Robotics and Automation Letters*, vol. 5, no. 2, pp. 3634–3641, 2020.

[16] D. Kim, H. Woo, Y. Ji, Y. Tamura, A. Yamashita, and H. Asama, "3D radiation imaging using mobile robot equipped with radiation detector," in *2017 IEEE/SICE International Symposium on System Integration (SII)*, 2017, pp. 444–449.

[17] D. Hellfeld, P. Barton, D. Gunter, A. Haefner, L. Mihailescu, and K. Vetter, "Real-Time Free-Moving Active Coded Mask 3D Gamma-Ray Imaging," *IEEE Transactions on Nuclear Science*, vol. 66, no. 10, pp. 2252–2260, 2019.

[18] A. Haefner, R. Barnowski, P. Luke, M. Amman, and K. Vetter, "Handheld real-time volumetric 3-D gamma-ray imaging," *Nuclear Instruments and Methods in Physics Research Section A: Accelerators, Spectrometers, Detectors and Associated Equipment*, vol. 857, pp. 42–49, 2017.

[19] T. Baca, M. Jilek, P. Manek, P. Stibinger, V. Linhart, J. Jakubek, and M. Saska, "Timepix radiation detector for autonomous radiation localization and mapping by micro unmanned vehicles," in *2019 IEEE/RSJ International Conference on Intelligent Robots and Systems (IROS)*, 2019, pp. 1129–1136.

[20] J. R. Schwank, "Basic mechanisms of radiation effects in the natural space radiation environment," Jun. 1994. [Online]. Available: `https://www.osti.gov/biblio/10158182`.

[21] T. Poikela, J. Plosila, T. Westerlund, M. Campbell, M Gaspari, X. Llopart, V Gromov, R. Kluit, M. van Beuzekom, F. Zappon, V Zivkovic, C. Brezina, K Desch, Y. Fu, and A Kruth, "Timepix3: A 65K channel hybrid pixel readout chip with simultaneous ToA/ToT and sparse readout," *Journal of Instrumentation*, vol. 9, p. C05013, May 2014.

[22] M. Quigley, K. Conley, B. Gerkey, J. Faust, T. Foote, J. Leibs, R. Wheeler, and A. Ng, "ROS: an open-source Robot Operating System," *ICRA Workshop on Open Source Software*, vol. 3, Jan. 2009.

[23] T. Baca, M. Petrlik, M. Vrba, V. Spurny, R. Penicka, D. Hert, and M. Saska, "The MRS UAV System: Pushing the Frontiers of Reproducible Research, Real-world Deployment, and Education with Autonomous Unmanned Aerial Vehicles," *Journal of Intelligent & Robotic Systems*, vol. 102, no. 26, pp. 1–28, 1 May 2021.

[24] X. Lojacono, "Image reconstruction for Compton camera with application to hadrontherapy," Theses, INSA de Lyon, Nov. 2013. [Online]. Available: `https://theses.hal.science/tel-01081066`.

[0] M. Frandes, B. Timar, and D. Lungeanu, "Image Reconstruction Techniques for Compton Scattering Based Imaging: An Overview [Compton Based Image Reconstruction Approaches]," *Current Medical Imaging Reviews*, vol. 12, no. 2, pp. 95–105, Mar. 2016.

[25] L. A. Shepp and Y. Vardi, "Maximum Likelihood Reconstruction for Emission Tomography," *IEEE Transactions on Medical Imaging*, vol. 1, no. 2, pp. 113–122, Oct. 1982.

[26] K. Lange and R. Carson, "EM Reconstruction Algorithms for Emission and Transmission Tomography," *Journal of computer assisted tomography*, vol. 8, pp. 306–316, May 1984.

[27] S. Wilderman, N. Clinthorne, J. Fessler, C.-H. Hua, and W. Rogers, "List Mode EM Reconstruction of Compton Scatter Camera Images in 3-D," vol. 2, Feb. 2000, 15/292 –15/295 vol.2.

[28] A. Andreyev, A. Sitek, and A. Celler, "Stochastic Image Reconstruction Method for Compton Camera," *IEEE Nuclear Science Symposium Conference Record*, pp. 2985 –2988, Dec. 2009.

[29] S. Wilderman, N. Clinthorne, J. Fessler, and W. Rogers, "List-mode maximum likelihood reconstruction of Compton scatter camera images in nuclear medicine," in *1998 IEEE Nuclear Science Symposium Conference Record. 1998 IEEE Nuclear Science Symposium and Medical Imaging Conference (Cat. No.98CH36255)*, vol. 3, 1998, 1716–1720 vol.3.

[30] A. P. Dempster, N. M. Laird, and D. B. Rubin, "Maximum Likelihood from Incomplete Data via the EM Algorithm," *Journal of the Royal Statistical Society. Series B (Methodological)*, vol. 39, no. 1, pp. 1–38, 1977.

[31] S. Wilderman, J. Fessler, N. Clinthorne, J. LeBlanc, and W. Rogers, "Improved Modeling of System Response in List Mode EM Reconstruction of Compton Scatter Camera Images," *Nuclear Science, IEEE Transactions on*, vol. 48, pp. 111 –116, Mar. 2001.

[32] V. Maxim, X. Lojacono, E. Hilaire, J. Krimmer, E. Testa, D. Dauvergne, I. Magnin, and R. Prost, "Probabilistic models and numerical calculation of system matrix and sensitivity in list-mode Mlem 3D reconstruction of Compton Camera Images," *Physics in Medicine and Biology*, vol. 61, no. 1, 243–264, 2015.

[33] Y. Feng, "Modeling and regularization in tomographic reconstruction for Compton camera imaging," PhD thesis, Universite de Lyon, 2020. [Online]. Available: `https://theses.hal.science/tel-02900652`.

[34] C. Ordonez and A. Bolozdynya, "Dependence of angular uncertainties on the energy resolution of Compton cameras," in *1997 IEEE Nuclear Science Symposium Conference Record*, vol. 2, Dec. 1997, 1122 –1125 vol.2.

[35] S. Lloyd, "Least squares quantization in PCM," *IEEE Transactions on Information Theory*, vol. 28, no. 2, pp. 129–137, 1982.

[36] P. Bradley, K. Bennett, and A. Demiriz, "Constrained K-Means Clustering," Aug. 2000. [Online]. Available: `https://www.researchgate.net/publication/2458036_Constrained_K-Means_Clustering`.

Chapter A

List of attachments

The `zip` file attached to the electronic version of this thesis in the KOS system contains source codes for proposed software methods organized into following subfolders:

- `mlem_radiation_mapping` — ROS node for mapping of ionizing radiation and planning future movement of the UAVs
- `monte_carlo` — code for simulation of the properties of the MiniPIX3 sensor
- `drone_data_sender` – ROS node for sending data between the UAVs and the ground station
- `astar_multiplaner` — ROS node for non-collision path planning
- and other helper functions.